Abstract

Title of Thesis:	DEVELOPMENT AND IN-SITU CHARACTERIZATION OF BI-LAYERED LAMINATED COMPOSITES FOR ENHANCED MOISTURE BARRIER PERFORMANCE Ibaad Gandikota, Master of Science, 2023
Thesis Directed By:	Professor Patrick McCluskey, Mechanical Engineering

Silicone encapsulations are widely used in high-temperature electronic applications, providing excellent properties like thermal stability, high purity, and chemical resistance. However, silicone is susceptible to moisture-induced failures due to high moisture permeability. This study mainly focuses on improving the moisture ingression characteristics of the silicone encapsulation by adding a polyurethane moisture barrier layer. This study focuses on the effects of moisture ingression by adding polyurethane and testing with embedded relative humidity sensors at different environmental conditions. The diffusivity of both the bi-layered composites and the pure encapsulation materials was assessed using two distinct experimental methods for the calculation of diffusivity based on the principles of 1-dimensional Fick's law of diffusion. The diffusivities were statistically analyzed to determine significant differences between the samples, and the experiment yielded a minimum of 65% reduction in diffusivity across the samples. Furthermore, a thermomechanical analysis was performed on two different GaN power

MOSFETs by the application of different underfill and potting encapsulations to determine stresses and strains on the solder bumps.

DEVELOPMENT AND IN-SITU CHARACTERIZATION OF BI-LAYERED LAMINATED COMPOSITES FOR ENHANCED MOISTURE BARRIER PERFORMANCE

By

Ibaad Gandikota

Thesis submitted to the Faculty of the Graduate School of the
University of Maryland, College Park, in partial fulfillment
of the requirements for the degree of
Master of Science
2023

Advisory Committee:

Professor Patrick McCluskey

Professor Abhijit Dasgupta

Professor Peter Sandborn

Acknowledgments

I wish to begin by expressing my deep gratitude to my advisor, Prof. McCluskey, whose unwavering support, profound expertise, and dedication to academic excellence have been instrumental in shaping the trajectory of this thesis. Their mentorship has been an invaluable inspiration and guidance throughout this journey.

I extend my heartfelt appreciation to my thesis committee members, Prof. Dasgupta and Prof. Sandborn, for their invaluable insights and feedback to ensure the quality and rigor of my research. Their collective wisdom has been pivotal in refining my work.

I am profoundly thankful to the members of my lab, Dr. Nave, Dr. Ahuja, Dr. Yun, Dr. Yao, and Cliff, whose collaboration, expertise, and camaraderie have played a pivotal role in the success of my research. The shared experiences and collective pursuit of knowledge in our lab have been a constant source of inspiration.

To my colleagues and friends from CALCE and the University of Maryland, including Veeresh, Lekhith, Abhishek, Chintan, Lokesh, Nikhil, Aniketh, Micheal, Megin, Mrugesh, Bhargav, Yi Hsieh, and Dinesh, their unwavering support, encouragement, and understanding during the challenging phases of this journey have been a source of strength. Their belief in me has motivated me, and I am grateful for our cherished moments.

Last but certainly not least, I extend my most profound appreciation to my family. My parents, my siblings, and their families, especially my nieces and nephews, their love, encouragement, and sacrifices have been the bedrock upon which this endeavor was built. Your unwavering faith in my abilities and support have sustained me throughout.

This thesis culminates in these exceptional individuals' collective support, guidance, and encouragement. With profound gratitude, I acknowledge their contributions to this work.

Table of Contents

Acknowledgments ii

1. Introduction 1
   - 1.1. Effects of Water on Electronics 3
     - 1.1.1. Leakage Current by Water Ingress 4
     - 1.1.2. Corrosion 4
     - 1.1.3. Degradation of Polymeric Material 7
   - 1.2. Encapsulation Materials 8
     - 1.2.1. Moisture Failures in Silicone Gel Encapsulation 10
   - 1.3. Scope of Thesis 13
2. Literature Review 14
   - 2.1. Experimental Techniques to Measure Moisture Ingression 14
     - 2.1.1. Water Vapor Transmission Rate 15
     - 2.1.2. Measurement of Moisture Content with Weight Gain 17
     - 2.1.3. In-situ Measurements with Embedded Sensors 19
     - 2.1.4. Synopsis of Techniques to Measure Moisture Ingression 19
   - 2.2. Moisture Barrier Techniques for Silicone 20
3. Experimental Setup 24

3.1. Bi-Layered Encapsulation Preparation 24

3.2. PCB Design 26

3.3. Solder Reflow 28

3.4. Multiplexer Design and Data Logging 31

3.5. Design of Experiments 32

4. Results and Discussions 34

4.1. Experimental Results 34

4.1.1. Material Degradation 37

4.1.2. Delamination of Protective Layer 40

4.2. Diffusion Modelling 42

4.2.1. ANOVA Analysis of Diffusivity 48

4.3. Failure Analysis and Thermomechanical Analysis of GaN Devices 51

4.3.1. Failure Analysis of GaN MOSFETs 51

4.3.2. Thermo-mechanical Parametric Investigation of Potting Materials 52

5. Contributions and Future Work 59

5.1. Contributions 59

5.2. Future Work 59

Appendix 61

Arduino script for Multiplexer 61

References 69

List of Tables

Table 1 Moisture-based Failure mechanism of distinct electronic components [3] 4

Table 2: Properties of common Encapsulation Materials [5], [7]... 9

Table 3: WVTR of different encapsulation materials for PV modules 16

Table 4: Parameters for the Langmuir-type model to describe moisture absorption [25]. 21

Table 5: Oven inputs for the Reflow Profile.. 29

Table 6: Individual sample division for Design of Experiments 34

Table 7: Calculated Diffusivities of samples in different methods.. 44

Table 8: ANOVA for Diffusivity with Moisture Content at 85-85 Test 48

Table 9: ANOVA for Diffusivity with RH at 85-85 Test... 48

Table 10: ANOVA for Diffusivity with Moisture content at 50-60 Test 49

Table 11: ANOVA for Diffusivity with RH at 50-60 Test.. 49

List of Figures

Figure 1 : Copernicus Climate Change Service using ERA5 hourly data for the calendar year 2022 3

Figure 2: Galvanic corrosion examples. (a) Galvanic corrosion between the aluminum bond pad and gold bond ball, (b) Galvanic corrosion in the underlying nickel layer and the gold surface in hearing aids, (c) Creep corrosion in silver-finished boards 6

Figure 3: Electrolytic Corrosion Examples. (a) dendrite formation in a ceramic capacitor, and (b) Formation of the conductive film in plater through holes in a PCB 7

Figure 4: (a) Interfacial delamination between copper trace and solder mask in PBGA Packages, and (b) Void growth in hygroscopic swelling due to water 8

Figure 5: Corrosion in Silicone gel encapsulated IGBT Modules. (a) copper and silver dendrite formation at the JT, and (b) eroded metallization due to aluminum corrosion 11

Figure 6: Failure in Silicone gel encapsulated silicon nitride IGBT module 12

Figure 7: Water vapor bubble formation in silicone gel encapsulation for silicon carbide power modules 13

Figure 8: Fickian and Non-Fickian Moisture Diffusion 14

Figure 9: WVTR of composite encapsulation materials for improved moisture diffusion characteristics. (a) PEN and graphene-induced PEN composites, and (b) PTPT and SiO_2-PTPT composite 17

Figure 10: Experimentally evaluated moisture content of (a) plastic package and (b) organic laminates. 18

Figure 11: SEM cross-sectional images of surface fluorinated samples [23] 21

Figure 12: Results from the studies in [24]. (a) SEM images of fractured surfaces of silicone composite, (b) WVTR properties of Silicone composite with various TiO2 content.................. 22

Figure 13: Package structure for LSI chips.. 23

Figure 14: Homogenous contact between silicone and polyurethane encapsulation.................. 25

Figure 15: Circuit diagram for BPS 240 sensors. Schematic design in eagle cad for (b) Sensor board and (c) Controller Board 27

Figure 16: PCB layout of (a) Sensor board and (b) Controller Board 28

Figure 17: (a) Reflow assembly of RH sensors (b) Recommended reflow profile in the data sheet (c) Comparison between recommended and experimental reflow profiles. 30

Figure 18: Schematic design of the testing setup.. 32

Figure 19: Cross-sectional Layout of Samples 33

Figure 20: Relative Humidity of the Samples at (a) 85°C-85% RH (b) 50°C-60% RH............... 36

Figure 21: Moisture Content (%) of the Samples at (a) 85°C-85% RH (b) 50°C-60% RH 39

Figure 22: Delamination in Cx samples at (a) 85°C-85% RH and (b) 50°C-60% RH................ 41

Figure 23: Delamination in Cy samples at 85°C-85% RH 42

Figure 24: Curve Fitting using RH Diffusivity of the Samples at (a) 85°C-85% RH and (b) 50°C-60% RH.. 46

Figure 25: Curve Fitting using Moisture Content Diffusivity of the Samples at (a) 85°C-85% RH and (b) 50°C-60% RH... 48

Figure 26: Post hoc analysis using the Tukey-Kramer method for Diffusivity at 85-85 Test with (a) Moisture Content and (b) RH 50

Figure 27: Post hoc analysis using the Tukey-Kramer method for Diffusivity at 50-60 Test with (a) Moisture Content and (b) RH 50

Figure 28: Failure Analysis of GaN MOSFETs to locate the delaminated solder bumps............ 52

Figure 29: Modelling and meshing of GaN Devices (a) Assembly, (b) EPC2001C solder bumps, and (c) EPC2204 solder bumps.. 55

Figure 30: Simulation results of GaN switches (a) Deformation, (b) Normal stress, and (c) Shear stress.. 58

1. Introduction

Water and electricity are both characterized by “flow” and are critical to our existence. Electronics have become ubiquitous and vital to us, yet water and electronics do not mix well. The impact of water on electronic function can be catastrophic, from the impact on data transmission to the potential hazards associated with shorts and malfunctions.

Electronics, especially the ones used for outdoor applications, are highly susceptible to interaction with moisture. For example, in the case of PV modules for residential applications, especially inverters, which are generally installed outside. This practice directly exposes the inverters to the atmosphere. These electronic modules can reach temperatures above 100°C during their operational time (i.e., sunrise to sunset.) However, these modules are turned off in the night, due to a lack of sunlight and the atmospheric relative humidity increases, making the modules susceptible to moisture ingression.

To understand the atmospheric behavior, the temperature and relative humidity data of California's center (longitudinally and latitudinally) has been collected from the Copernicus Climate Change Service using ERA5 hourly data for the calendar year 2022, as shown in Figure 1. In the off-summer seasons, the atmospheric relative humidity is above 70% at night [1].

Based on the effects of the climate, the nights have a more significant impact in terms of moisture. This study focuses on developing techniques to mitigate moisture-induced failure in the electronics based on the phenomena mentioned in this chapter, along with other moisture-induced effects on electronics.

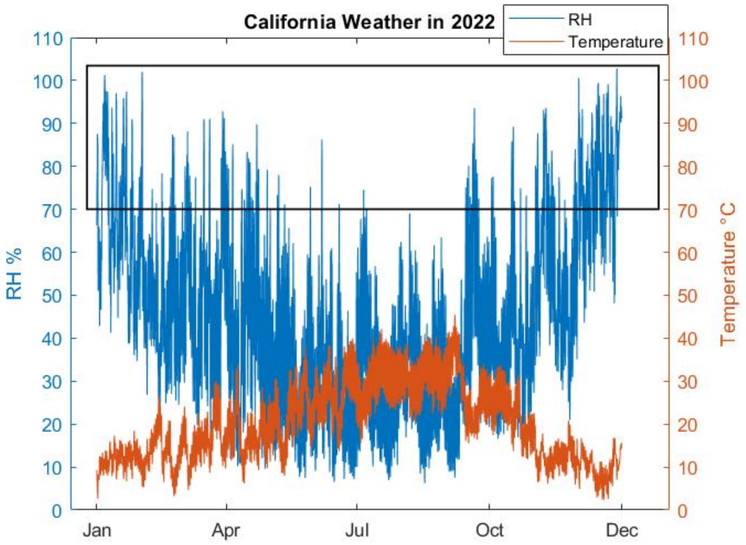
California Weather in 2022
RH
Temperature
RH %
Temperature °C
0
10
20
30
40
50
60
70
80
90
100
110
Jan
Apr
Jul
Oct
Dec

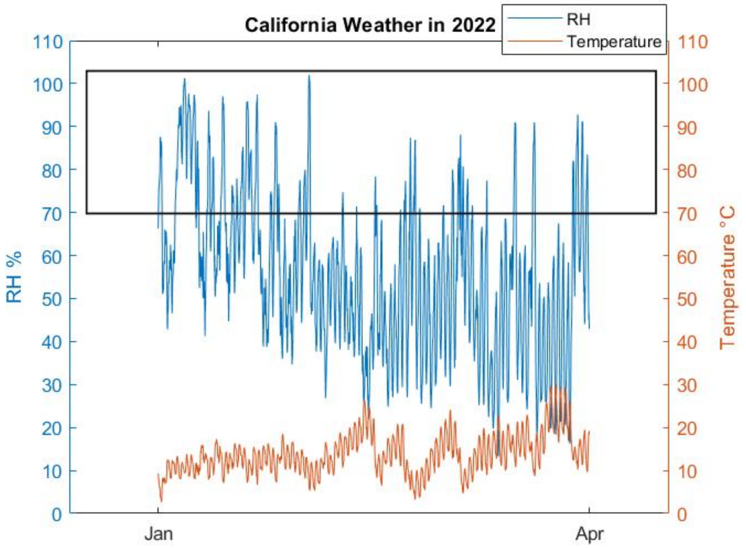
California Weather in 2022
RH
Temperature
RH %
Temperature °C
0
10
20
30
40
50
60
70
80
90
100
110
Jan
Apr

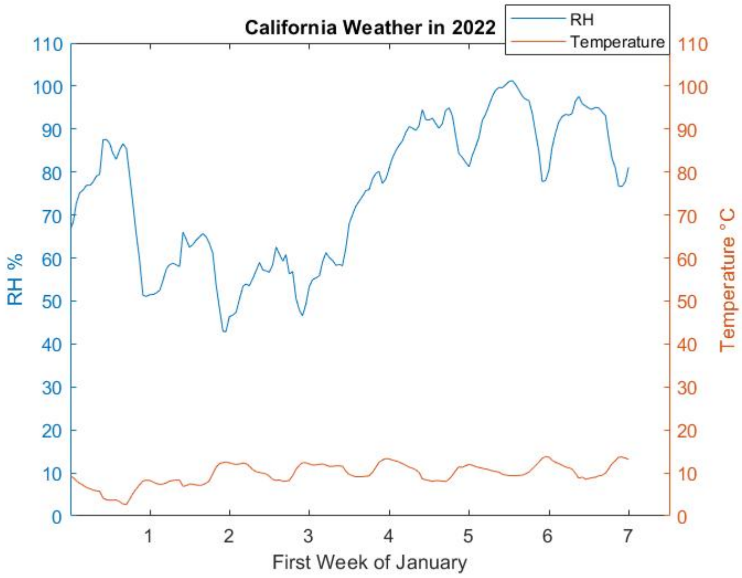

Figure 1 : Copernicus Climate Change Service using ERA5 hourly data for the calendar year 2022

1.1. Effects of Water on Electronics

To fulfill its targeted application, an electronic device needs to operate at the given operating environmental conditions. This means an electronic device must withstand electrical, mechanical, and thermal stresses. Though IC manufacturing companies mainly perform thermal, thermo-mechanical, vibration, and impact tests for a given device, the effects of moisture/water are often neglected [2]. Except in non-hermetic packages, moisture can affect almost every electronic package, such as hygroscopic polymeric materials (e.g., solder resist, dielectric, encapsulation.) Moisture can penetrate through these materials, causing failures of different components like printed circuit boards (PCB), die metallization, molding compound, capacitors / film capacitors, transistors, conductive adhesives, and films. A few of the well-known failure mechanisms caused by water interaction with the components mentioned are shown in Table 1[3].

Failure Mechanisms	Affected Components
leakage current by water ingress	capacitor/film capacitor, printed circuit boards
corrosion	transistor, die metallization, conductive adhesive, printed circuit boards, capacitor/film capacitor
dielectric loss	capacitor/film capacitor
material degradation	anisotropic conductive film, nonconductive adhesive, molding compound, printed circuit boards
delamination/crack	anisotropic conductive film, nonconductive adhesive, molding compound, printed circuit boards

Table 1 Moisture-based Failure mechanism of distinct electronic components [3]

1.1.1. Leakage Current by Water Ingress

The interaction of water with electronics can create an unwanted conductive path where the electrons tend to flow, causing leakage currents. These leakage currents are generally observed on the non-conductive parts of electronic components. This adversely impacts the functionality of the electronic component—for instance, the leakage current in polymer aluminum electrolytic capacitors increases with an increase in moisture ingress. The capacitors were tested in high-temperature and high relative humidity (RH) environment (85°C-85% RH), causing the leakage current to go over the failure criterion of the design specification of leakage currents [4].

1.1.2. Corrosion

Corrosion incorporates all material-environment reactions, regardless of the reaction's scope or the rates of its initial and subsequent stages. Generally, corrosion is an irreversible mechanism where moisture-related corrosion underlies the electrochemical process. This electrochemical process is divided into galvanic corrosion and electrolytic corrosion.

Galvanic corrosion occurs when a moisture layer connects two dissimilar metals where moisture behaves like an electrolyte between a cathode and anode, causing electrochemical migration. For example, this electrolytic behavior can cause corrosion between aluminum and gold by forming metal oxides, as shown in Figure 1(a). Similarly, another example of battery contact on gold-finished electroplated nickel in the presence of water caused cracking, delamination, and formation of pores, as shown in Figure 1(b). Galvanic corrosion also occurs in conductive adhesives, typically affecting metal particles and epoxy moldings. Due to the hygroscopic nature of epoxy, it tends to absorb moisture, causing corrosion onto the metallic parts. Creep corrosion is another type of galvanic corrosion where silver or gold finished boards interact with sulfur gas in the presence of water, forming an acidic electrolyte and promoting corrosion. This process is generally accelerated by the carboxylic acid in the solder flux for better solder wettability, as shown in Figure 1(c).

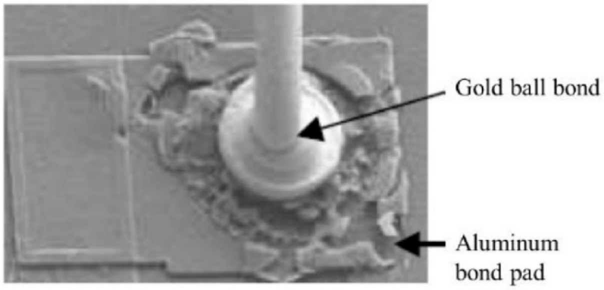

(a)

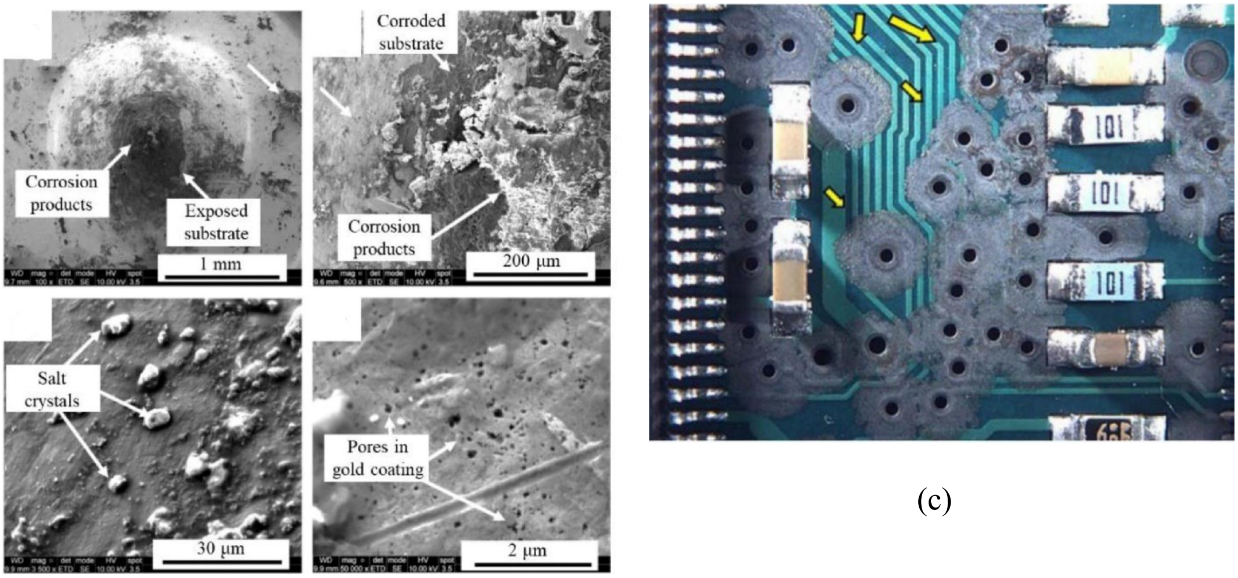

(c)

(b)

Figure 2: Galvanic corrosion examples. (a) Galvanic corrosion between the aluminum bond pad and gold bond ball, (b) Galvanic corrosion in the underlying nickel layer and the gold surface in hearing aids, (c) Creep corrosion in silver-finished boards

Electrolytic corrosion differs slightly from galvanic corrosion, where a water film connects two biased conductors, creating a conductive path between them. In this electrochemical migration, a corrosion-driven conductive path is formed between insulating material between the two conductors. For instance, the conductive path was developed as a conductive dendrite in a ceramic capacitor, or a conductive anodic filament was formed between plated-through-holes in a PCB, as shown in Figure 2.

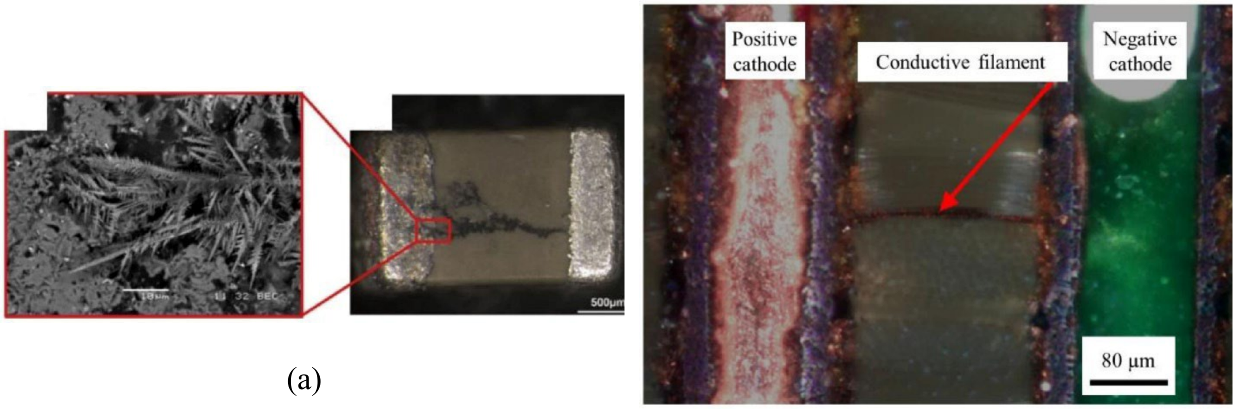

(a)

(b)

Figure 3: Electrolytic Corrosion Examples. (a) dendrite formation in a ceramic capacitor, and (b) Formation of the conductive film in plater through holes in a PCB

1.1.3. Degradation of Polymeric Material

Moisture absorption into polymeric materials can disrupt intermolecular interactions of polymeric chains. This can change the physical properties like volume, fracture toughness, and elastic modulus of the polymeric compound.

In the case of polymeric adhesives, moisture can interact with residual chemicals in adhesives to form acids. These acids interact with the material, causing degradation of interfacial adhesion. In a different case, moisture can occupy spaces inside the adhesives. When these components are reflowed for assembly, the vapor pressure of the water increases due to high reflow temperature, causing delamination or cracks at the interface, as shown in Figure 3 (a).

Moisture ingression can also cause swelling of the polymeric materials. The water occupies the volume in polymeric voids and slowly expands these voids; as it occupies the empty spaces in the polymeric chains, it tends to stretch these spaces, eventually causing swelling. This hygroscopic swelling can lead to mismatches causing warpage, leading to failure. Figure 3 (b) demonstrates the void expansion in polymeric materials.

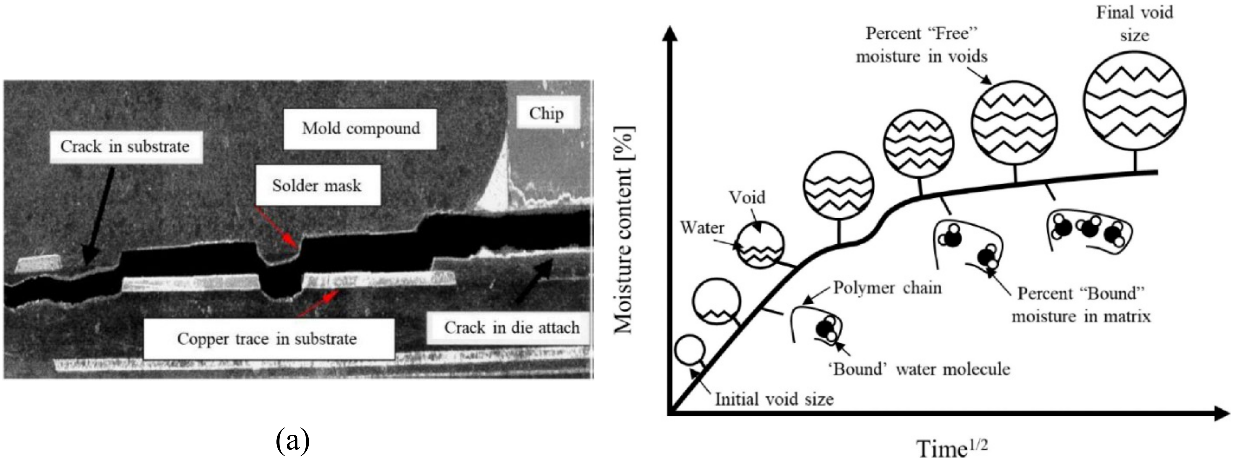

(a)

(b)

Figure 4: (a) Interfacial delamination between copper trace and solder mask in PBGA Packages, and (b) Void growth in hygroscopic swelling due to water

1.2. Encapsulation Materials

Minimizing moisture ingress is an imperative part of manufacturing electronic devices. Generally, a chip is encapsulated using techniques like molding, glob top, and underfill until the assembly is complete. Additional protection is provided by applying conformal coating or potting encapsulation over the assembled printed circuit board (PCB). Conformal coating is a thin (25 to 125 μm) semi-hermitic layer applied onto the assembly, where these layers protect the assembly from environmental agents like moisture, sulfides and chlorides. Another method is potting encapsulation, a protection method where electronic assemblies are entirely submerged under soft/rigid potting encapsulation materials. This technique protects against coefficient of thermal expansion (CTE) mismatch, shock, vibration, moisture, electrical breakdown, corrosive agents, etc. The most common materials used for electronic encapsulation are epoxy resins, urethanes, and silicone gels, which have advantages and disadvantages, as shown in Table 2 [3], [5]–[7].

Material	Advantages	Disadvantages
Epoxy	• Good chemical and mechanical protection • Suitable for all thermosetting processing methods • Excellent wetting characteristics • Ability to cure at atmospheric pressure. • Excellent adhesion • Low Cost	• High stress • Moisture sensitive • Short shelf life • Shrinkage during curing • Brittle at low temperatures
Silicone	• Low stresses • Excellent electrical properties • Good chemical resistance • Low water absorption • Thermal stability up to 315°C • Good UV resistance	• Low tensile tear strength • High cost • Attacked by halogenated solvents. • Poor adhesion • Long cure time
Polyurethane	• Good mechanical properties (toughness, flexibility, resistance to abrasion) • Low viscosity • Low moisture absorption • Ambient curing possible • Thermal stability up to 135°C • Low cost	• Poor thermal stability • Poor weatherability • Flammable • Dark color • High ionic concentration

Table 2: Properties of common Encapsulation Materials [5], [7]

Even though both silicone and polyurethane have excellent moisture-resistant properties, polyurethane has the edge over silicones as silicones tend to “breathe moisture,” where moisture can easily flow in and out of the material, but it doesn’t store moisture, i.e., silicones have higher moisture permeability [8]. This behavior would not directly raise dielectric breakdowns but can corrode the chip within the encapsulation. However, due to high-temperature stability and low glass transition temperature (T_g), silicone gel is an ideal encapsulation choice for high-temperature electronic applications. Further, the softness of silicone gel raises minute stresses while curing and can absorb stresses due to coefficient of thermal expansion (CTE) mismatches [5], [9], [10].

1.2.1. Moisture Failures in Silicone Gel Encapsulation

Silicone encapsulation compounds do not exhibit complete impermeability to moisture. Water vapor can penetrate through the silicone encapsulations, causing moisture-induced failures. Different failure mechanisms were observed for silicone gel encapsulation in the literature, some of which were stated in this section.

The temperature humidity bias test was performed for 1000 hours at 85°C and 85% Relative Humidity (RH) on various 1200V and 1700V IGBT modules. The junction termination (JT) is affected by the formation of a closed water film, which acts as an electrolytic solution linking the active chip metallization area and channel stopper metallization. In this scenario, active chip metallization acts as a negative electrode (cathode), and stopper metallization acts as a positive electrode (anode). Mechanisms like galvanic electrochemical migration and aluminum corrosion were observed in the IGBT modules. Electrochemical Migration was observed in the form of copper and silver dendrites at the JT, which transported the direct bonded copper and solder, as shown in Figure 4 (a) [11]. Another study by Zorn et al. [12] also observed corrosion at the aluminum metallization on the JT, where the active aluminum was seen to be corroded. In this phenomenon, an acidic solution of aluminum hydroxide ($Al(OH)_3$) was observed with the interaction with water; this acidic solution further interacted with the metallization forming aluminates, as shown in Figure 4(b) [12].

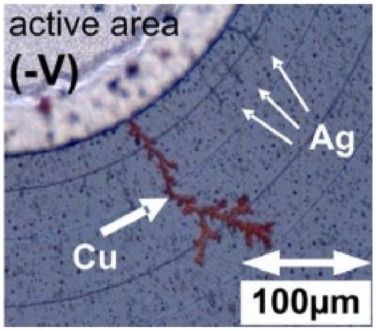

1.7 kV module

(a)

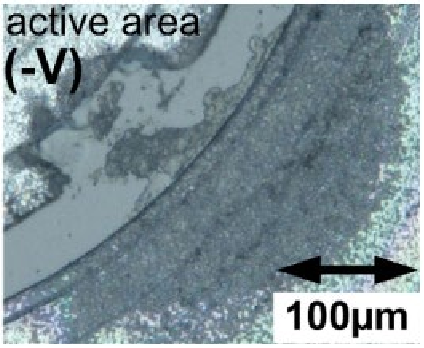

1.2 kV module

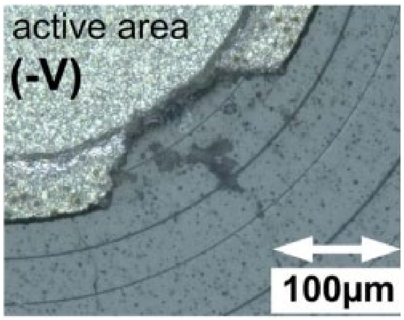

1.7 kV module

(b)

Figure 5: Corrosion in Silicone gel encapsulated IGBT Modules. (a) copper and silver dendrite formation at the JT, and (b) eroded metallization due to aluminum corrosion

Similar to the previous study, Papadopoulos et al. [13] also tested IGBT modules for 1000 hours at 85°C and 85% RH, along with an applied reverse bias voltage of 80 V. The IGBT was encapsulated with silicone gel over two layers of passivation, where the first layer was silicon nitride passivation, and the second layer was polyamide passivation. The investigation into the failure analysis revealed corrosion in the gate runner aluminum and delamination of the polyamide passivation. Further, corrosion was also observed in the first layer of passivation of silicon nitride, which was transformed into silicon dioxide, as shown in Figure 5 [13].

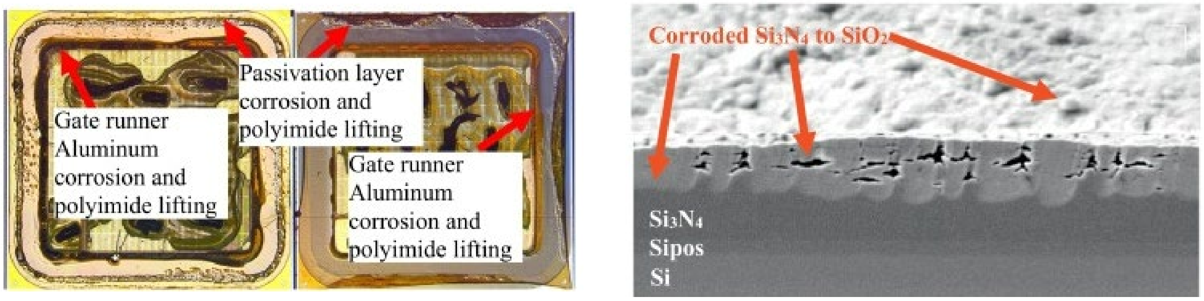

Figure 6: Failure in Silicone gel encapsulated silicon nitride IGBT module

In a different study, SiC MOSFETs with silicone encapsulation were tested for void formation at the chip interface. The module was connected to a liquid cooling heat sink, which was connected to the base plate of the module. Temperature and RH sensors were embedded inside the encapsulation, ensuring the heat sink temperature would not fall under the air temperature in the module, confirming that the module does not form any dew. Testing was stopped after the saturation of the silicone gel, which was approved by the RH sensor. The modules were subjected to heavy loading, which raised the temperature of the chips, where void formation was observed. This void further expanded due to the release of moisture from the encapsulation, causing entanglement of the wire bond, eventually causing the failure of these chips, as shown in Figure 6 [14].

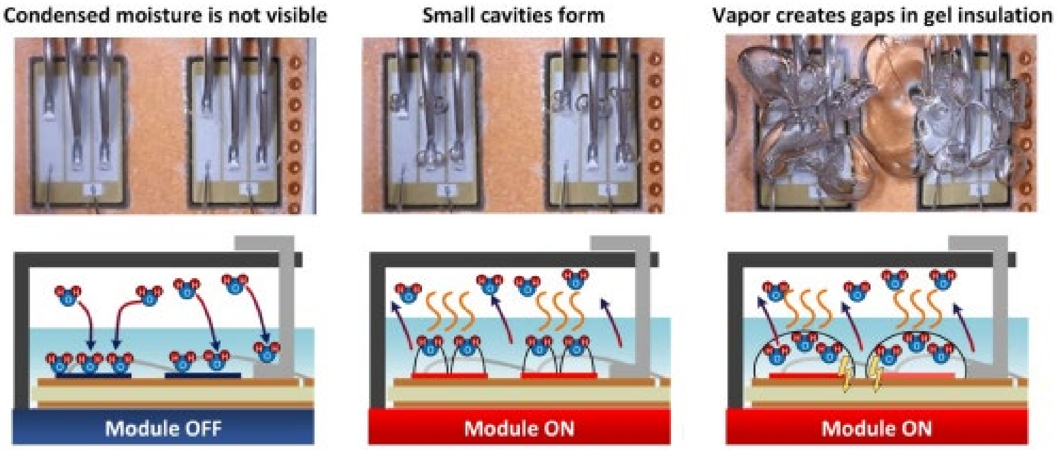

Figure 7: Water vapor bubble formation in silicone gel encapsulation for silicon carbide power modules

1.3. Scope of Thesis

It is crucial to understand how encapsulation affects electronic assemblies so one can pick the suitable material for the job. Based on the literature, it was found that silicone encapsulation is the best for high-temperature applications, yet it has some drawbacks due to high moisture permeability. This research aims to propose and characterize a simple and inexpensive polymeric moisture barrier that further mitigates moisture ingression through silicone. Furthermore, modeling analysis was conducted using a finite element analysis (FEA) model to observe the effects of potting onto assemblies of Gallium nitride (GaN) flip-chip power MOSFET modules, where a detailed parametric investigation was performed to determine the stresses and strains on solder bumps with different potting materials.

2. Literature Review

Since silicone encapsulation material is susceptible to moisture ingression, this research aims to fabricate a composite silicone encapsulation and experimentally determine moisture ingression through encapsulation. The literature review mainly focuses on experimental techniques to measure moisture ingression and a survey of methodologies intended to improve silicone gel moisture ingress characteristics.

2.1. Experimental Techniques to Measure Moisture Ingression

Polymeric materials can display different moisture diffusion characteristics. These characteristics are mainly divided into two categories: Fickian and non-Fickian trends. The Fickian diffusion model is an exponential equation that represents the moisture ingression with respect to time. In contrast, the non-Fickian model, where the polymeric material initially follows Fickian trends, but in the later stages, the moisture ingression rate slows down due to void growth. This implies that the complete sorption of moisture takes more extended time periods when compared to Fickian. Figure 7 demonstrates the different trends of Fickian and non-Fickian diffusion models [7].

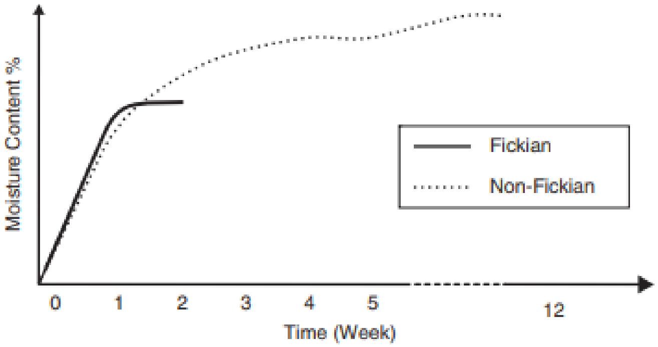

Figure 8: Fickian and Non-Fickian Moisture Diffusion

Polymeric materials are tested using various techniques in a specified humidity and time. The polymeric materials are tested by thoroughly soaking them. These materials are tested to determine the percentage of weight gain. In these tests, the materials are submerged in boiling water for 24 hours or submerged in distilled water at room temperature for 24 hours. Another common practice to characterize the material is calculating the diffusivity at 85°C and 85% RH. These environmental conditions are based on IPC/JDEC standards (IPC/JDEC J-STD-20, IPC Association Connecting Electronic Industries, and JEDEC Solid State Technology Association), where the moisture content is calculated. The ratio of weight change from a dry state to a wet state with dry state weight calculates the moisture content [7]. Several authors in the literature developed different methods to calculate moisture ingression; some of those techniques are discussed in the remainder of this chapter.

2.1.1. Water Vapor Transmission Rate

ASTM F1249 is one of the standard testing methods to measure the water vapor transmission rate (WVTR) through plastic films and sheets using a modulated infrared sensor. WVTR is the time rate of water vapor flow normal to the surface under steady-state conditions per unit area. The testing is performed in a sealed sample-separated dry and wet chambers. Water vapor diffuses from the wet chamber to the dry chamber through the sample material and mixes with the gas in the dry chamber. This causes a change in the pressure, where the pressure-modulated infrared sensor measures the fraction of infrared energy absorbed by the water vapor. After calibration of the sensor data, the WVTR of the given material is measured [15].

In the literature, the WVTR measurement test was performed on various encapsulation materials at different temperatures and relative humidities based on the ASTM standard. Jorgensen et al. [22] conducted a WVTR test for Photovoltaic (PV) module encapsulations, where different candidate materials for encapsulation, like EVA, PET, etc., were tested; in some cases, the materials were coated to improve the moisture ingress properties shown in Table 3 [16].

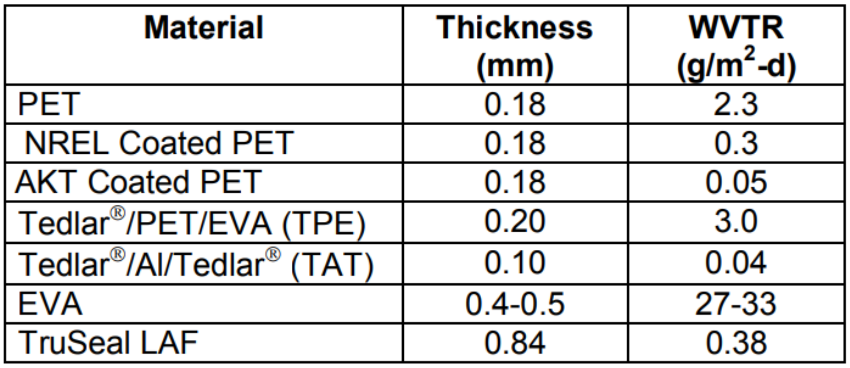

Material	**Thickness (mm)**	**WVTR (g/m^2-d)**
PET	0.18	2.3
NREL Coated PET	0.18	0.3
AKT Coated PET	0.18	0.05
Tedlar®/PET/EVA (TPE)	0.20	3.0
Tedlar®/Al/Tedlar® (TAT)	0.10	0.04
EVA	0.4-0.5	27-33
TruSeal LAF	0.84	0.38

Table 3: WVTR of different encapsulation materials for PV modules

In other studies, the WVTR test was performed for the assessment of moisture ingress improvements in reinforced composite encapsulation. Polyethylene naphthalate (PEN) was encapsulated with thin film barriers of graphene oxide for flexible photovoltaic modules for wearable applications. The introduction of graphene oxide films enhances the gas barrier properties of PEN encapsulation for PV modules. Figure 8 (a) demonstrates how the moisture ingress decreases with the increase in the thickness of the barrier layer, and the WVTR test was performed for two different temperatures of 25°C and 38°C at 100% RH [17]. In an alternative investigation, poly(trimethylolpropane triacrylate), also called PTPT encapsulant, was introduced with silicon dioxide nanoparticles infused, forming SiO_2-PTPT nanocomposite. The authors used the standard method to measure WVTR and found that introducing SiO_2 decreased the WVTR significantly, as shown in Figure 8 (b) [18].

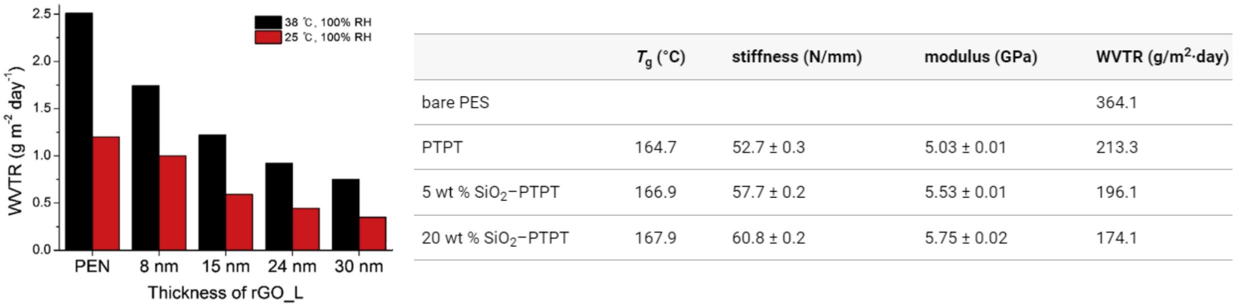

	T_g (°C)	stiffness (N/mm)	modulus (GPa)	WVTR (g/m^2·day)
bare PES				364.1
PTPT	164.7	52.7 ± 0.3	5.03 ± 0.01	213.3
5 wt % SiO_2–PTPT	166.9	57.7 ± 0.2	5.53 ± 0.01	196.1
20 wt % SiO_2–PTPT	167.9	60.8 ± 0.2	5.75 ± 0.02	174.1

(b)

(a)

Figure 9: WVTR of composite encapsulation materials for improved moisture diffusion characteristics. (a) PEN and graphene-induced PEN composites, and (b) PTPT and SiO_2-PTPT composite

2.1.2. Measurement of Moisture Content with Weight Gain

The percentage weight gain for a given time defines the moisture content inside a polymeric material. As mentioned before, it is the ratio of change in weight and weight in the dry state. Generally, polymeric materials are completely dehydrated until there is no change in the weight, i.e., the material is completely moisture-free. Subsequently, the materials are subjected to atmospheric conditions of temperature and humidity. This leads to moisture ingression into the material, where the weight of the sample is measured at regular intervals with a weighing scale.

Ardebili, H. et al. [19] carried out a moisture ingression test on plastic encapsulation materials, where these samples were molded into two different packages. The test was initiated by drying out the packages at 125°C for 24 hours and later subjected to 85°C and 85% RH environmental conditions. The weight gain measurements were experimentally plotted, and the results were theoretically fitted with 1-D Fick's law of diffusion, as shown in Figure 9(a). Similarly, another study was performed on organic laminates by Pecht et al. [20] on resins used in laminates. The moisture ingression within them again was characterized by the moisture content calculation, as shown in Figure 9(b).

In a different study, silicone gel encapsulation was tested for moisture ingression by calculating the moisture content of the sample. Similar to the previous studies, the samples were initially dehydrated and then subjected to environmental conditions of 85°C and 85% RH based on the JESD22-A101D.01 standard [21].

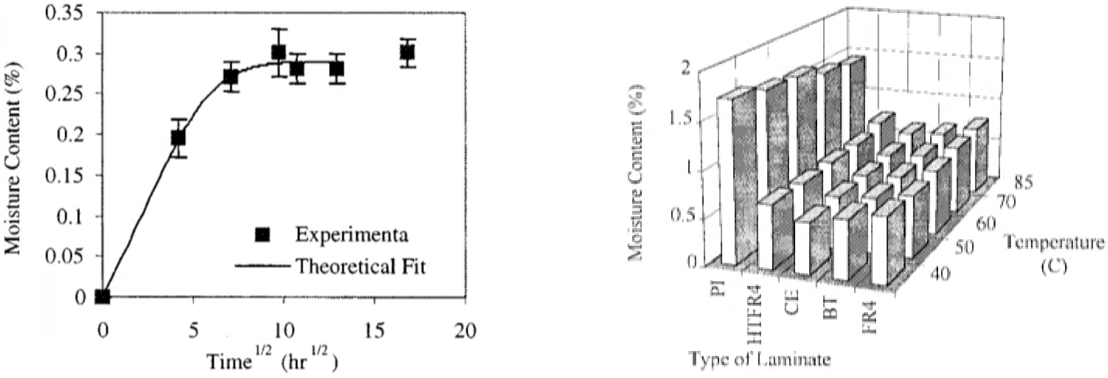

(a)

(b)

Figure 10: Experimentally evaluated moisture content of (a) plastic package and (b) organic laminates.

2.1.3. In-situ Measurements with Embedded Sensors

The in-situ moisture ingression behavior of an encapsulation material can be determined by embedding moisture-sensitive sensors inside the polymeric material. Sensors like capacitive moisture sensors, capacitive humidity sensors, etc., are embedded inside the polymeric material, and the materials are subjected to steady environmental conditions to measure the change in capacitance or change in RH. Similar to the previous method, the polymeric materials are initially dehydrated, and later, the load is applied to study the moisture ingression behavior of the material.

In previous studies, capacitive moisture sensors were encapsulated inside the mold, and the change in capacitance indicates the moisture ingression in the material [19]. In an alternative investigation, capacitive moisture sensors were replaced by relative humidity sensors [21]. Typically, the principle of relative humidity sensors is based on capacitive change with respect to the change in atmospheric relative humidity. Electrodes are separated by a hygroscopic dielectric film, which reacts to the water vapor in the atmosphere.

Different encapsulation materials like silicone gel, ethylene-vinyl-acetate (EVA), and epoxy have been tested with capacitance-based sensors. These sensors were embedded within the encapsulants, and these materials were tested based on the JESD22-A101D.01 standard at 85°C and 85% RH [19], [21]–[23],[24].

2.1.4. Synopsis of Techniques to Measure Moisture Ingression

Various techniques were utilized in the literature to characterize moisture ingression into various materials. Mainly, the change in percentage weight gain was demonstrated to understand the behavior of moisture ingress with time in environmental conditions of temperature and RH. This technique is simple and effective in demonstrating the voids occupied by the amount of free and bounded water molecules within the material. However, this technique does not account for the loss of water when the samples are returned to room temperature. Dynamic mass measurement with a precision of 0.1 mg is expensive, and condensation of water vapor can cause measurement discrepancies. In a different technique mentioned in this chapter, sensors were used to give in-situ moisture ingression characteristics. Capacitive or RH sensors were encapsulated with the test materials. Hence, moisture content measurement and embedded sensors were used to understand the behavior of moisture ingression in the materials used in this study.

2.2. Moisture Barrier Techniques for Silicone

In previous studies, various moisture barrier techniques were introduced where moisture diffusion was reduced significantly, and properties such as percentage moisture gain, diffusivity, and water vapor transmission rate (WVTR) were calculated. Zhenlian An et al. [25] introduced fluorine gas to create a moisture barrier over silicone rubber. The silicone rubber from Elkem Silicone Shanghai Co. was vulcanized at 200°C using 30% by weight of peroxide vulcanizing agent. The vulcanized silicone samples were cured with a thickness of 2 mm at 175°C. Each of the samples had the dimensions of 60 mm x 60 mm, and these samples were subjected to fluorine gas at 25°C, 55°C and 85°C which achieved fluorinated thicknesses of 0.56, 1.18, and 1.14 μm respectively, as shown in Figure 10. Since the samples did not follow the Fickian diffusion model, the samples were characterized using the Langmuir type model, and the diffusivities were more than 20% lower than virgin samples, as shown in Table 3 [25].

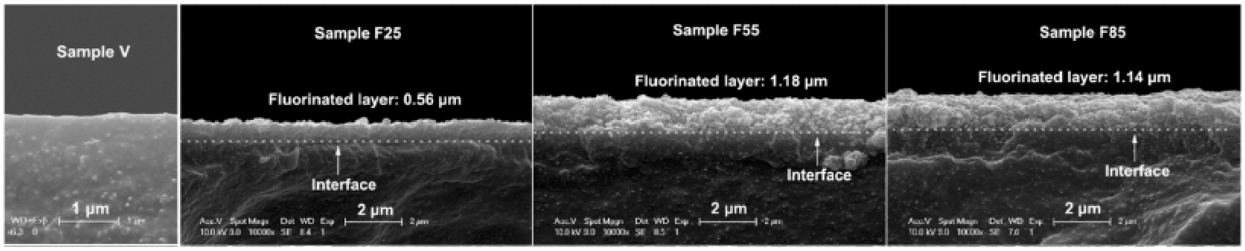

Figure 11: SEM cross-sectional images of surface fluorinated samples [23].

Sample	RH, temperature	m_∞, %	D, cm^2·s^{-1}	α , s^{-1}	β, s^{-1}
V	75%, 30°C	0.095	2.2×10^{-5}	1.3×10^{-4}	9.1×10^{-6}
	75%, 60°C	0.076	3.1×10^{-5}	1.2×10^{-4}	1.1×10^{-5}
	97%, 30°C	0.112	2.7×10^{-5}	1.8×10^{-4}	1.5×10^{-5}
	97%, 60°C	0.091	4.1×10^{-5}	2.3×10^{-4}	2.2×10^{-5}
F25	75%, 30°C	0.033	1.5×10^{-5}	8.9×10^{-5}	1.8×10^{-6}
F55	75%, 30°C	0.081	1.6×10^{-5}	3.3×10^{-4}	2.0×10^{-5}
F85	75%, 30°C	0.084	1.7×10^{-5}	2.1×10^{-5}	1.4×10^{-6}

Table 4: Parameters for the Langmuir-type model to describe moisture absorption [25].

In a different study, Liao et al. [26] improved the properties of silicone resin for high-temperature LED applications. This study aimed to decrease the moisture ingression into the silicone encapsulation and increase the refractive index (RI) of the silicone encapsulation by introducing inorganic nanoparticles with high RI. A composite was developed with the particle-reinforcement technique for silicone resin. Titanium dioxide (TiO_2) nanoparticles were further augmented by introducing tetramethoxyl silane (TMOS), creating silane-functionalized TiO_2 (TMOS-m-TiO_2). Both TiO_2 and silane-functionalized TiO_2 nanoparticles were employed as nanofillers for silicone. Sample dimensions were defined as 10 cm^2 with a thickness of 2 mm, and they were tested for WVTR at 40°C and 100% Relative Humidity (RH). Each sample set contained 0.01, 0.05, 0.10, and 0.15 phr (parts per hundred)of nanofiller, i.e., TiO_2 and TMOS-m-TiO_2.

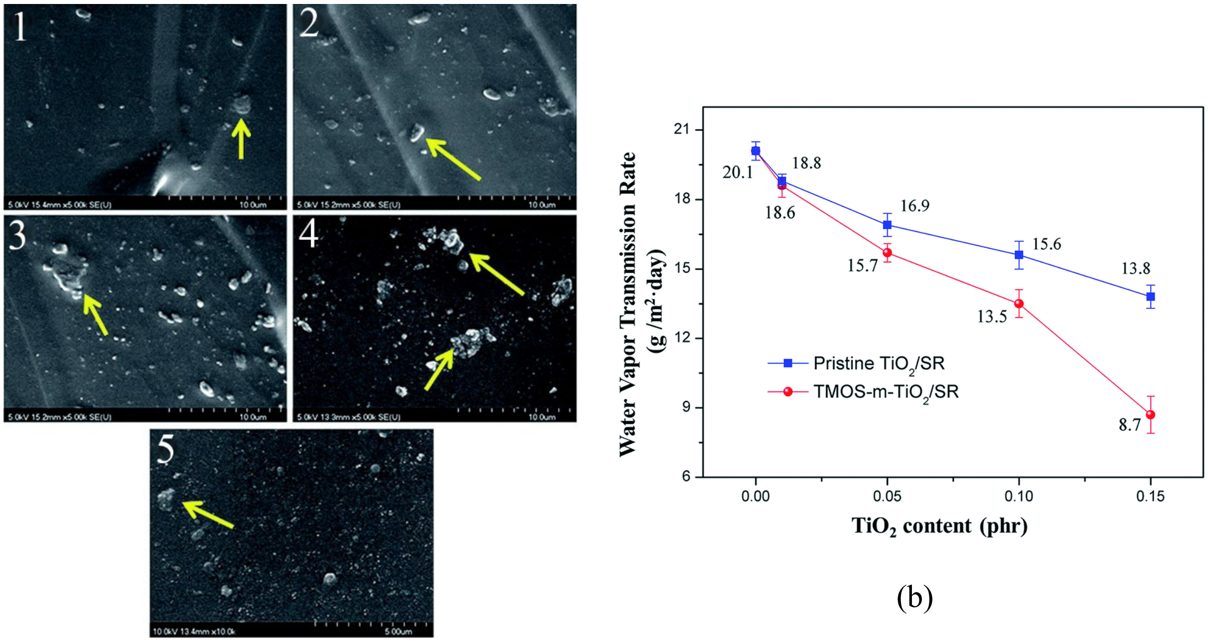

(b)

(a)

Figure 12: Results from the studies in [24]. (a) SEM images of fractured surfaces of silicone composite, (b) WVTR properties of Silicone composite with various TiO2 content.

Deposited nanofillers were studied using a scanning electron microscope. Images 1-4 in figure 11(a) represents 0.01, 0.05, 0.10 and 0.15 phr of TiO_2 whereas image 5 in Figure 11(b) represents 0.15 phr of TMOS-m-TiO_2. These images exhibit heterogeneity, formation of severe aggregation, and substantial roughness on the surface of the composite. Figure 11(b) demonstrates that the WVTR of these composites decreases as the amount of nanofiller increases. One can observe that silane-functionalized TiO_2 significantly decreases the WVTR over TiO_2 composite samples [26].

Lee et al. [27] also developed particle-reinforcement techniques to deposit graphene sheets into silicone encapsulation for LED applications. The graphene-based silicone composite was prepared using a solvent-exchange method, where graphene was deposited using ethanol. The sample sets were designed with a thickness of 5mm where 0.03, 0.06, 0.09, 0.12, and 0.15% wt of nanographene sheets were introduced. This study aimed to create a composite silicone encapsulation with superior thermal conductivity, high transmittance, and improving mechanical properties and barrier against moisture and sulfides. Each of these properties of silicone were improved, and the 0.15% wt graphene-based silicone had a water uptake of 0.24% wt, whereas the neat silicone had a water uptake of 0.27 % wt when the samples were soaked in water at 80°C [27].

In an alternative study, LSI chips were encapsulated with silicone gel with a concept called "chip floating," where all the material surrounding the chip is silicone gel. Further moisture protection was provided by the addition of an aluminum lid and aluminum frame, which was again attached with silicone gel with alumina fillers, as shown in Figure 12. This technique almost makes it a hermitic package except for the zones covered by the silicone gel interface. A pressurized cooker test (PCCT) was performed on the samples. Where the packages with lids attached did not show any signs of corrosion, moisture was discovered at the interface of the lid and silicone gel adhesive. In contrast, the packages without lids absorbed moisture, forming bubbles with the temperature changes, which led to the corrosion of the chips [8].

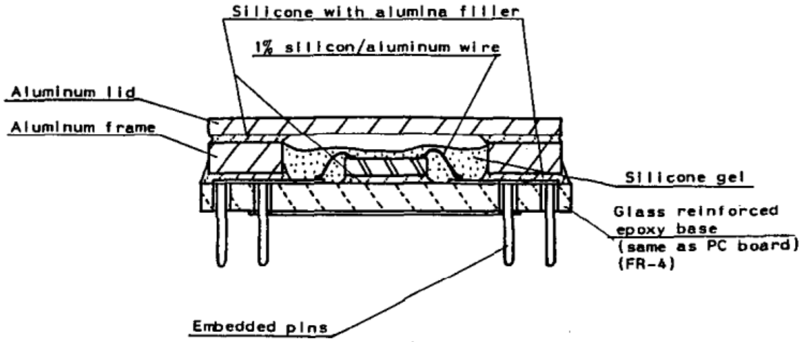

Figure 13: Package structure for LSI chips

Even though the moisture ingression was significantly reduced by the methods mentioned in the literature, each of these methods to create the encapsulation has its issues, such as higher cost, lower dielectric strength, and complex manufacturing process, which are unsuitable for power electronic modules. This research incorporated a simple and cost-effective solution to create a bi-layered laminated composite of silicone and polyurethane, where polyurethane acts as the moisture barrier. As mentioned in the previous chapter, polyurethanes are better at moisture prevention over silicones; hence, the polyurethane encapsulation material was selected for the moisture barrier.

3. Experimental Setup

In this chapter, the methodology for preparing the laminated composite of silicone and polyurethane is described in detail. As mentioned in the literature review, the testing techniques for moisture ingression were assessed. Temperature and RH sensors were embedded inside the encapsulation samples, along with the moisture content measurement. The change in mass was measured and tested for different environmental conditions. The process for creating the test setup and the methods to control automated data logging are also included.

3.1. Bi-Layered Encapsulation Preparation

The bi-layered composite was prepared using Dow SYLGARD 527 silicone gel and Epic Resins S7318 polyurethane. The design aimed to overcoat silicone gel with polyurethane, which acts as a moisture barrier. The main challenge with overcoating was to create a homogeneous interface between the laminates. Initially, it was observed that air bubbles formed in between the interfacial surfaces, which can trap water in them. These bubbles will store water; the stored water can be dormant or react with the polymer, making a hydrogen bond. These water molecules are in “free” and “bound” states, respectively. When the moisture increases with time, the bubbles will create void growth, causing swelling. This swelling can give rise to mismatches, causing warpage, eventually leading to failure of the composite. Multiple iterations were performed to eliminate these interfacial air bubbles, and the process that best worked to eliminate interfacial bubbles is discussed below.

Firstly, the two-part silicone was mixed in a 1:1 ratio by weight and degassed with GAST DAA-V711-E8 vacuum pump for 15 minutes in the sample cups. The two-part mixture was left to cure at room temperature for 48 hours. Later, two-part polyurethane was mixed in a separate container with a weight ratio of 100:16.8, and again, degassing was performed for another 15 minutes. Once the air bubbles were eliminated, the polyurethane mixture was carefully poured onto the cured silicone gel without accumulating any bubbles. Figure 13 demonstrates the elimination of air bubbles, and the orientation of the image is upside down as the silicone gel is evident over the black polyurethane polymer.

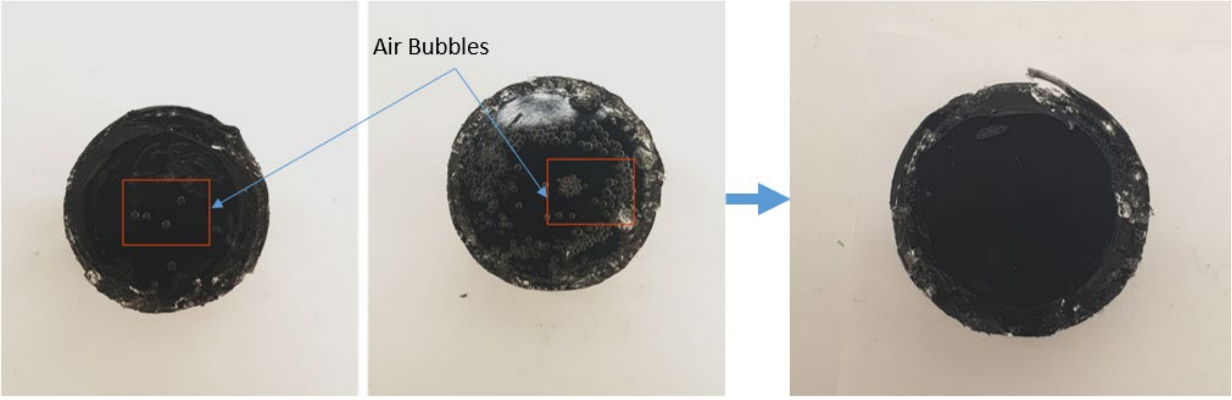

:

Figure 14: Homogenous contact between silicone and polyurethane encapsulation

3.2. PCB Design

The encapsulation materials were characterized using Bourns BPS240 temperature and RH sensors. BPS240 sensors are 2x2mm plastic dual flat, no lead package with six leads. These sensor chips need an Inter-Integrated Circuit (I2C) interface for communication and require passive components for data processing. Hence, two PCBs were designed using Eagle CAD to minimize the wiring, and they are defined as Sensor Board and Controller Board. Schematics of the sensor board were developed along with the footprint of the sensor based on the datasheet requirements, as shown in Figure 14. The schematic of the controller board was designed using EIA 0805 footprints for all the passive components, as shown in Figure 14. The SMD1,27-2,54 wire pads were used to connect the boards with wires based on the design requirements.

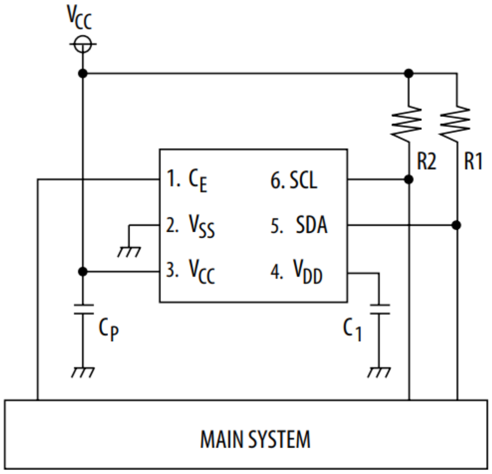

(a)

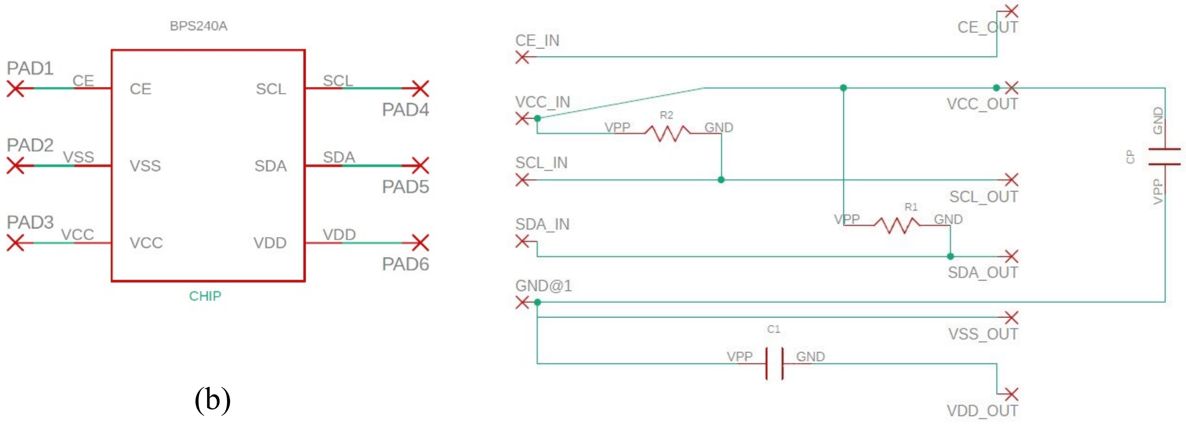

(b)

(c)

Figure 15: Circuit diagram for BPS 240 sensors. Schematic design in eagle cad for (b) Sensor board and (c) Controller Board

The schematics were used to generate board footprints, adjusted to achieve the required board design. The sensor was mounted on a 10x10 mm single-layer PCB, whereas the controller had two layers with dimensions of 26x20 mm, as shown in Figure 15. The circuit pins and circuit designs will be explained in Chapter 3.4.

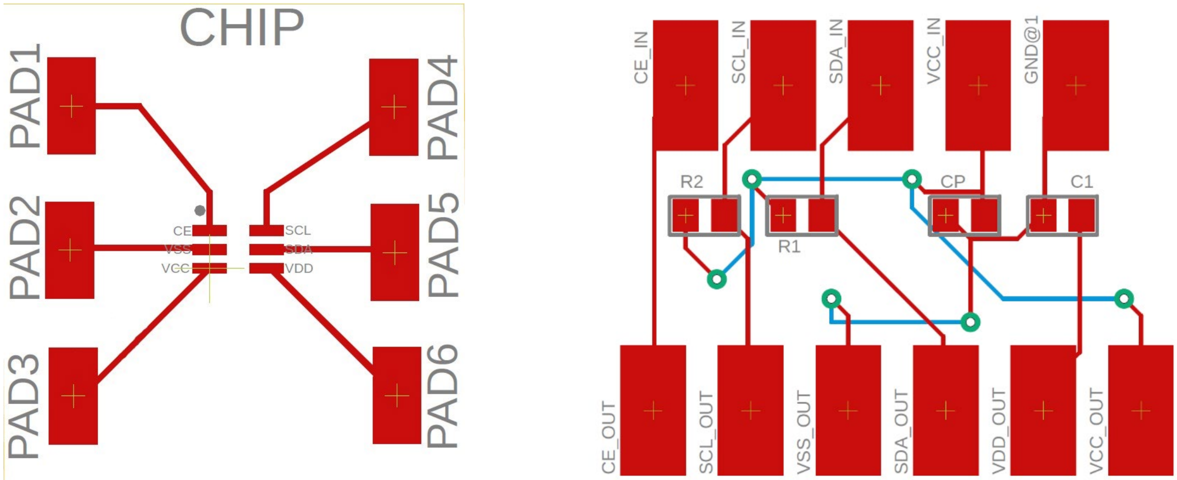

(a)

(b)

Figure 16: PCB layout of (a) Sensor board and (b) Controller Board

3.3. Solder Reflow

The designs of PCBs were fabricated with FR-4 as base material and copper with 1 oz thickness. The components were assembled using Indium8.9 Pb-Free Solder Paste in the DDM Novastar GF-125 Five Zone Benchtop Reflow Oven. The PCBs were assembled following the datasheet of the solder paste recommended solder profiles, as shown in Figure 16 (a). The most common reflow profiles used for reflowing are called Linear Profile or Delta-Type profile and Soak profile or trapezoidal profile. The selection of the profile depends on the assembly components; simple assemblies can be soldered with delta-type reflow profiles, whereas the assemblies with complex or large components like BGAs can create large deviations in thermal mass where the preferred profile is the trapezoidal-type profile for reflow [28], [29]. Due to the small components in the assembly, the delta-type solder profile was selected for soldering.

The reflow profile was achieved by connecting a K-type thermocouple to a sample PCB placed on an aluminum plate. This sample board was reflowed for multiple iterations until the reflow profile was achieved. The reflow oven was set to a combination of natural and forced convection in the five reflow zones, and the belt speed was as shown in Table 4. However, due to the five temperature zones, the soaking was slightly lower than the actual profile. The assembly was completed using the achieved profile, and the assembly process is mentioned as follows. The solder paste was applied onto the copper pads with the help of stencils designed for the boards, and then the components were carefully placed on the solder paste. The wetting forces of liquidus solder tend to pull the component to correct its alignment; hence, the reflow process corrects misalignments [30]

Zones	Zone 1	Zone 2	Zone 3	Zone 4	Zone 5	Cooling zone
Temperature (°C)	169	220	245	235	285	Room Temp
Fan Speed	0	40	60	0	100	100

Table 5: Oven inputs for the Reflow Profile

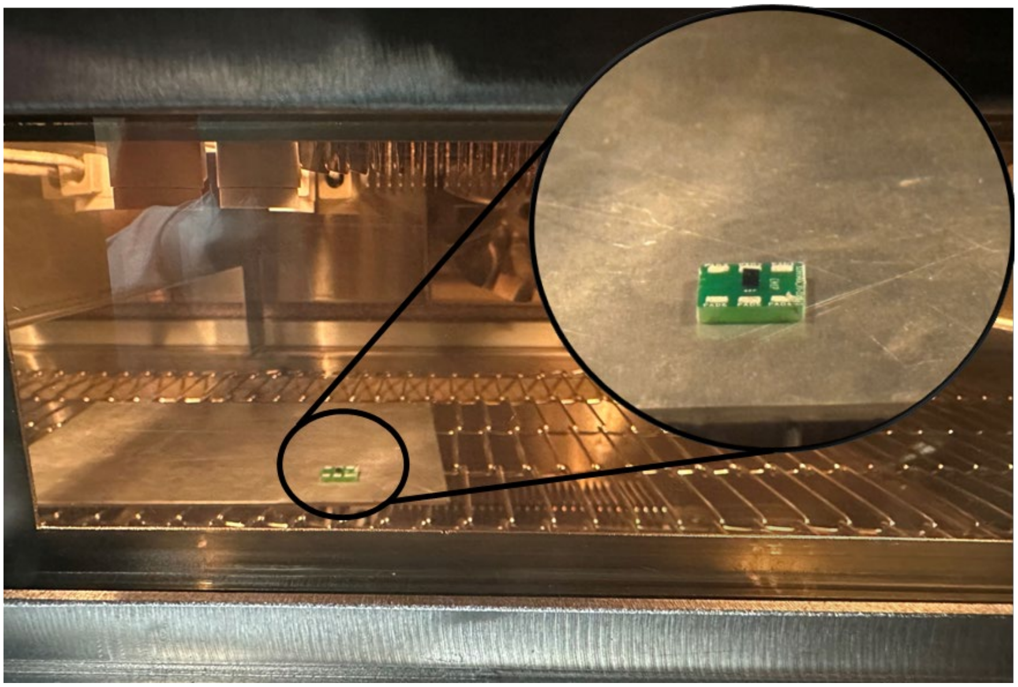

(a)

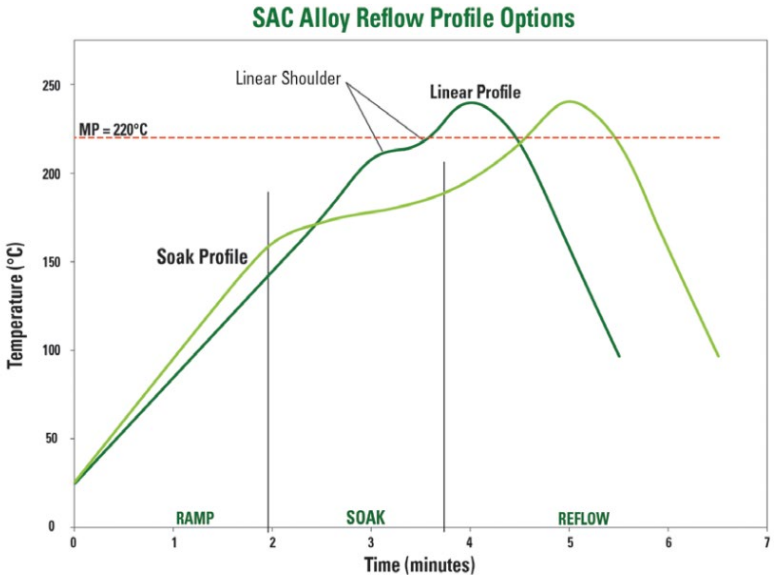

(b)

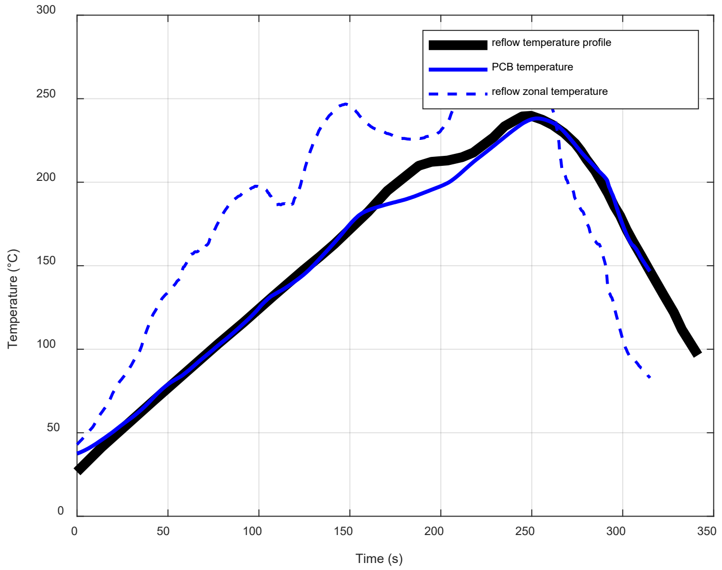

(c)

Figure 17: (a) Reflow assembly of RH sensors (b) Recommended reflow profile in the data sheet (c) Comparison between recommended and experimental reflow profiles.

3.4. Multiplexer Design and Data Logging

I2C protocol is a two-way method for serial communication for sensing, where there is interaction between multiple masters and multiple slaves. In this research, the master device is Arduino MEGA, and slaves are the BPS 240 sensors. The significant advantage of the I2C protocol is that it reduces the total pins required for data logging, where two common lines are used to communicate without any data loss. These common lines are called Serial Data (SDA) and Serial Clock (SCL), where SDA is bidirectional, whereas SCL is unidirectional. The master STARTs the protocol, and the SDA line moves from high to low and is later followed by SCL. Once the protocol has begun, the device continuously sends the data. Pull-up resistors are connected to these lines for power supply, and the resistance is dependent upon the number of slave devices; the number of slaves goes up, then resistance is decreased. Generally, a unique 7-bit address is assigned to the slave where the data is stored, and this data can be processed from the serial data line [31].

Along with these typical characteristics of the I2C protocol, the BPS 240 has a Chip Enable switch, which controls whether the device is turned on or off. Based on the chip enable feature, the multiplexing of the system was designed, where the data was collected only when the CE was in a high state. Each of these sensors were assigned to a digital pin in Arduino MEGA, and a loop was created to collect data when the digital pin output was on high. All the other pins were merged with the help of a terminal block, forming a single node, as shown in Figure 17. These nodes were then connected to the controller board. The power supply, ground, SCL, and SDA pins from the Arduino were connected to the other side of the controller board.

The RH and Temperature data were recorded using a Microsoft EXCEL feature called data streamer. The data was recorded every 10 seconds, i.e., every data logging cycle happened after a delay of 10 seconds, and each of the subsequent sensors recorded the data at a time interval of 1 second. There is a 0.05-second delay in recording temperature and RH within one sample. The experimentation was performed based on the mentioned timings for data logging.

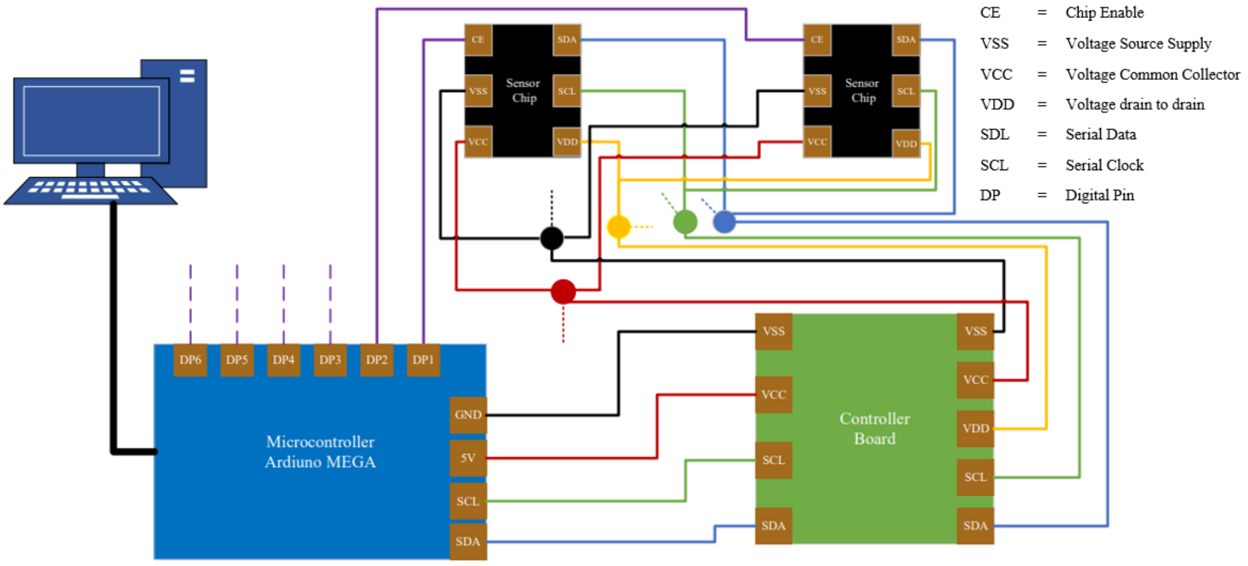

Figure 18: Schematic design of the testing setup.

3.5. Design of Experiments

The encapsulation material, silicone, polyurethane, and their composite were cured in aluminum cups. The aluminum sample cups were selected to eliminate any moisture penetration from the sides and the bottom, exposing only the top surface of the encapsulation. These cups, with a diameter of 73 mm and a depth of 17.5 mm, were chosen for the experimentation.

The total height of the sample encapsulation was specified at 12 mm, where samples of silicone, polyurethane, composite x (Cx), and composite y (Cy) were cured inside the aluminum cups. Silicone and polyurethane samples were encapsulated at a height of 12 mm, whereas the Cx was encapsulated with 8 mm of silicone and 4 mm of polyurethane. Contrastingly, Cy was encapsulated with 4 mm of silicone and 8 mm of polyurethane, as shown in Figure 18. Sample sets of four for each encapsulation type mentioned above were employed for the testing, making a total of 16 samples per test, as shown in Table 5.

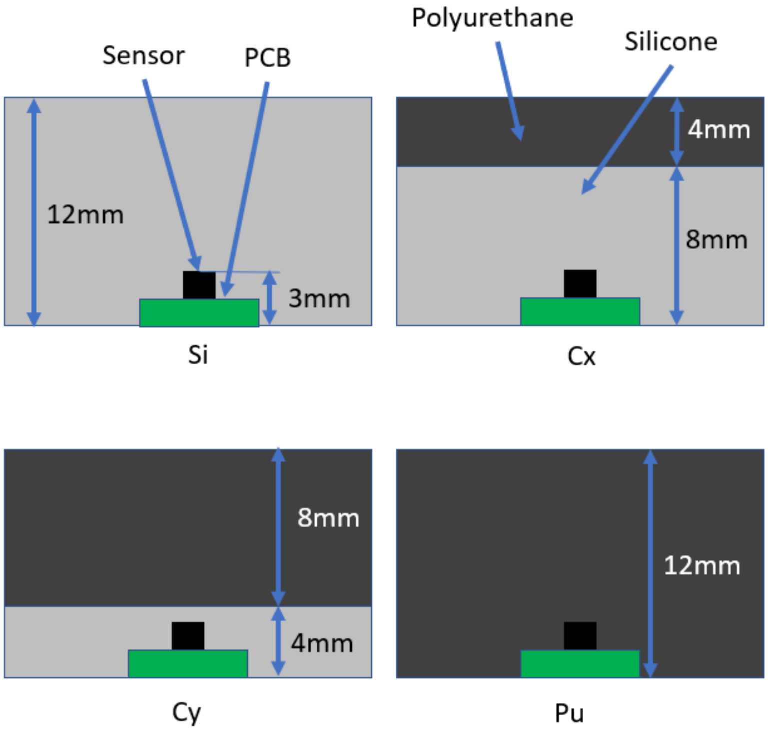

Figure 19: Cross-sectional Layout of Samples

Sample Sets				
Sample Composition (mm)	Si 12/Pu 0	Si 8/Pu 4	Si 4/ Pu 8	Si 0/ Pu 12
Samples Names	Si 1	Cx 1	Cy 1	Pu 1
	Si 2	Cx 2	Cy 2	Pu 2
	Si 3	Cx 3	Cy 3	Pu 3
	Si 4	Cx 4	Cy 4	Pu 4

Table 6: Individual sample division for Design of Experiments

After the curing, all 16 samples were dehydrated in Sun Electronics EC12 temperature chamber for 24 hours. The ramp rate was 0.5°C/min, and the dwell temperature was 125°C, as shown in Figure 18. The test was performed under two different environmental conditions. Initially, the JEDEC JESD22-A101D.01 standard was used for the environmental conditions of 85°C and 85% RH. This standard is used for non-hermetic packages to employ accelerated moisture penetration through encapsulation with high temperature and humidity conditions. Later, the environmental conditions were reduced to 50°C and 60% RH to study the moisture ingression, reducing the acceleration factor.

4. Results and Discussions

Based on the testing techniques and testing environments, the results obtained are discussed in this chapter. The experimental results and theoretical modeling using Fick's law were graphically represented along with the calculation of the diffusivities. A statistical comparison was performed on the diffusivities using ANOVA analysis. Further, thermo-mechanical analysis was also performed on the GaN MOSFETs to compare the effects of the application of different potting and underfill encapsulations.

4.1. Experimental Results

The experiments were carried out in ESPEC PRA-3AP standard Temperature/Humidity chamber. The relative humidity profile inside the encapsulation material was obtained for both the environmental conditions of 85°C-85% RH and 50°C-60% RH to understand the behavior of the composite and pure encapsulation materials, as shown in Figure 19. The change in the relative humidity based on the difference in the time was recorded until the samples reached an equilibrium with the surroundings, i.e., the applied testing condition.

The anomalous dip, as seen in Fig 19(a), in the first test was caused by the tripping of the circuit breaker fuse of the humidifier of the chamber for a couple of hours. Once identified, the humidifier was again turned back on.

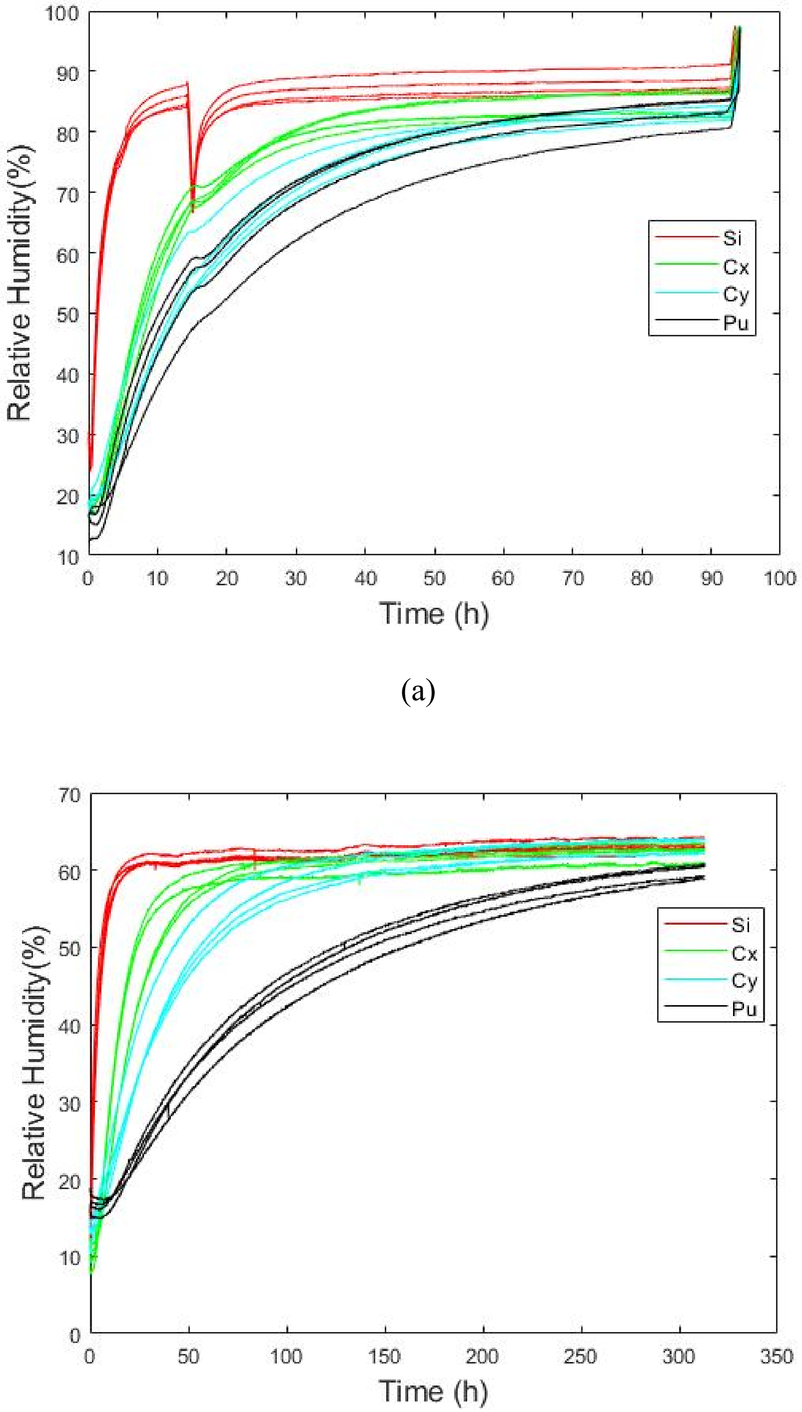

(a)

(b)

Figure 20: Relative Humidity of the Samples at (a) 85°C-85% RH (b) 50°C-60% RH

In the first test (85°C-85% RH), it can be observed that the samples saturate within a span of 100 hours, whereas in the second test (50°C-60% RH), it took more than 300 hours for all the samples to saturate. This variation in time required for saturation could be attributed to higher temperature acceleration in the first test. Cy and Pu samples follow a similar trajectory in the first test, whereas in the second test, Cy and Pu samples follow a different course. This pattern implies that polyurethane performance improves significantly at lower temperatures.

Based on the obtained trends, it could also be that the application of a polyurethane layer to silicone gel significantly reduces the rate of change in RH when compared to pure silicone gel packages. Thus, it can be implied that the moisture ingress performance increases in the order of Si, Cx, Cy, and Pu respectively.

4.1.1. Material Degradation

To assess the degradation of the moisture absorption capability due to prolonged exposure at higher temperatures, the weight of the samples was measured prior to the start of the test and after the complete saturation. Subsequently, the samples were allowed to soak further in the testing chamber after sample saturation. The samples were removed from the chamber at regular intervals, and their weight was recorded. The change in the weight of the samples could be attributed to the change in the moisture content in the encapsulation.

The trend of percentage change in the moisture content at different time intervals is captured in Figure 20. The percentage change in sample weight was evaluated with the weight of the sample at the start of the test as the reference. As shown in Figure 20(a), the initial increment in the weight until 100 hours corresponds to the moisture absorbed by the potting to reach the saturation conditions. During the prolonged exposure after sample saturation, the potting material tends to release moisture, which could be attributed to the degradation of the ability of the material to hold the absorbed moisture. A similar trend was also observed in the second test.

In a comparison of the two tests, the moisture content in the sample at saturation in the first test was significantly higher, almost twice that of the second test. This was observed due to higher environmental temperature and humidity, and the overall moisture absorption in the first test was found to be higher.

However, soaking the samples in the saturation conditions further, the moisture content after reaching the saturation tends to decrease, and after 400 hours of testing in 85°C-85% RH condition, the weight of the samples was found to be lower than the weight found in the initial dehydrated state. A similar trend was also observed by testing in 50°C-60% RH. This implies that both silicone and polyurethane materials have degraded with time. In literature, it was found that moisture absorption causes the material to lose its weight.

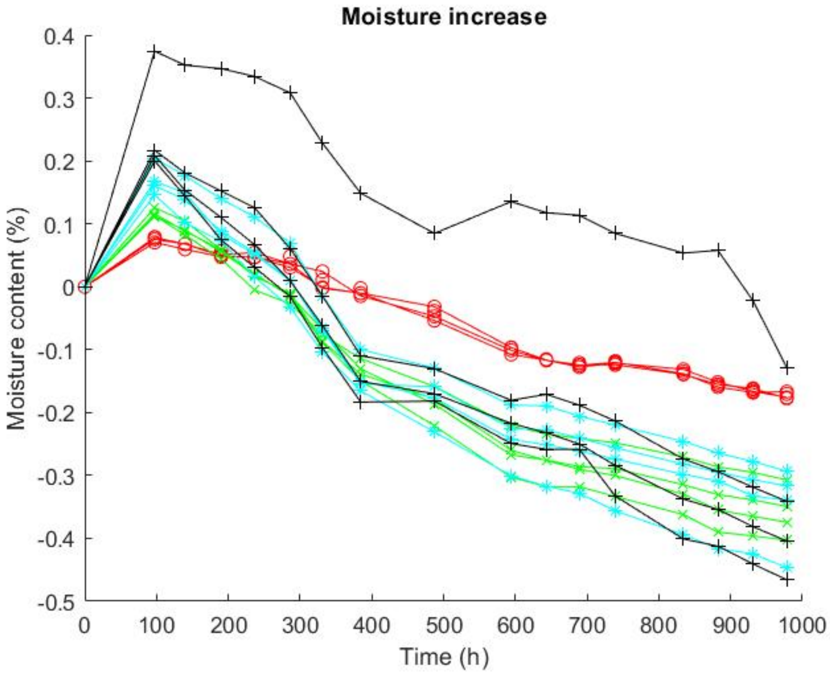

(a)

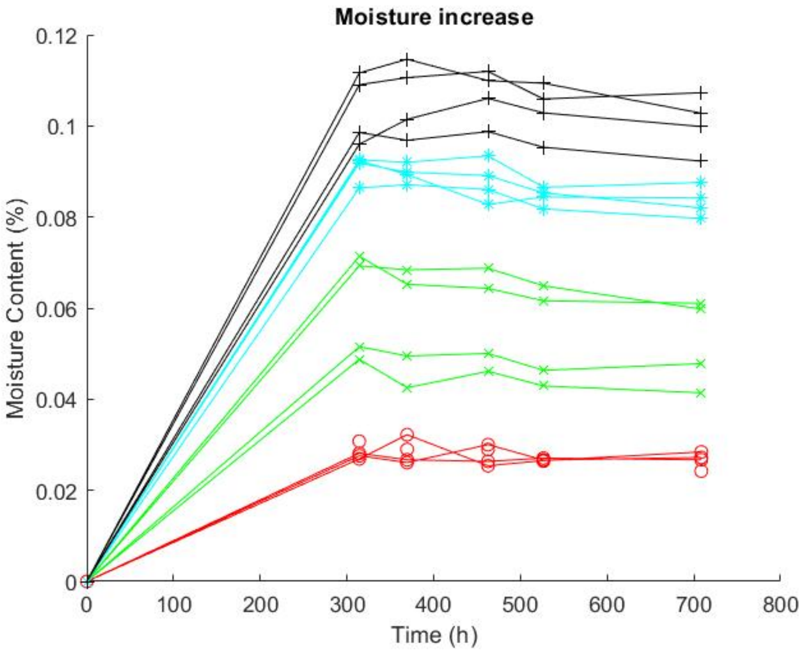

(b)

Figure 21: Moisture Content (%) of the Samples at (a) 85°C-85% RH (b) 50°C-60% RH

To understand the degradation phenomenon, which is the mass loss in the materials, a review of a study performed by et al. Li has been mentioned for silicone degradation. The structure in silicone gel is a dimethyl siloxane cross-link network where the gaps between the linkages are occupied by siloxane with vinyl and siloxane with hydrogen. During the moisture absorption phase, these small siloxane molecules dissolve into water with hydrogen bonding. Due to interdiffusion, the dissolved water molecules are replaced by clean water. This causes mass loss even when the actual moisture increases. This phenomenon depends mainly on the glass transition temperature (T_g). If the atmospheric temperature is lower than T_g, then moisture is transported in a fixed path. Since the cross-linked polymeric chain does not dissolve in moisture, it isolates small siloxane molecules from dissolving in water. However, when the temperature exceeds T_g, the moisture can travel freely through different channels into the voids occupied by the siloxane, causing a reaction between water and siloxane molecules. Due to this free travel, more siloxane reacts with the water, causing mass loss [21].

Based on the assessment above, it can be said that the materials experience mass loss while they are experiencing high temperatures and humidity. Thus, it can be inferred that the moisture content method to analyze the moisture ingression into these materials does not account for the mass loss. In chapter 4.2, further analysis is performed to demonstrate how the absence of mass loss of the material due to degradation can cause discrepancies in the moisture ingression for soft materials.

4.1.2. Delamination of Protective Layer

While the sample was removed from the testing chamber to measure their weight, a visual inspection of the samples was also done to identify any potential delamination of potting material with respect to the sample holder (aluminum cup). Delamination of the polyurethane layer was observed in Cx and Cy samples after saturation in both 85°C-85% RH and 50°C-60% RH tests.

In Figure 21, the delamination is observed at the edges of the aluminum cup, where the contact between the polyurethane and aluminum is 4 mm. Unlike Cx samples, where complete delamination from the edges was found, Cy samples delaminated only at specific regions. Based on Figure 21 and Figure 22, a permanent deformation was observed on the aluminum cups, which reveals that CTE mismatches and hygroscopic swelling of the materials caused the delamination of the polyurethane layer. The application of additives can enhance adhesion to counteract this phenomenon.

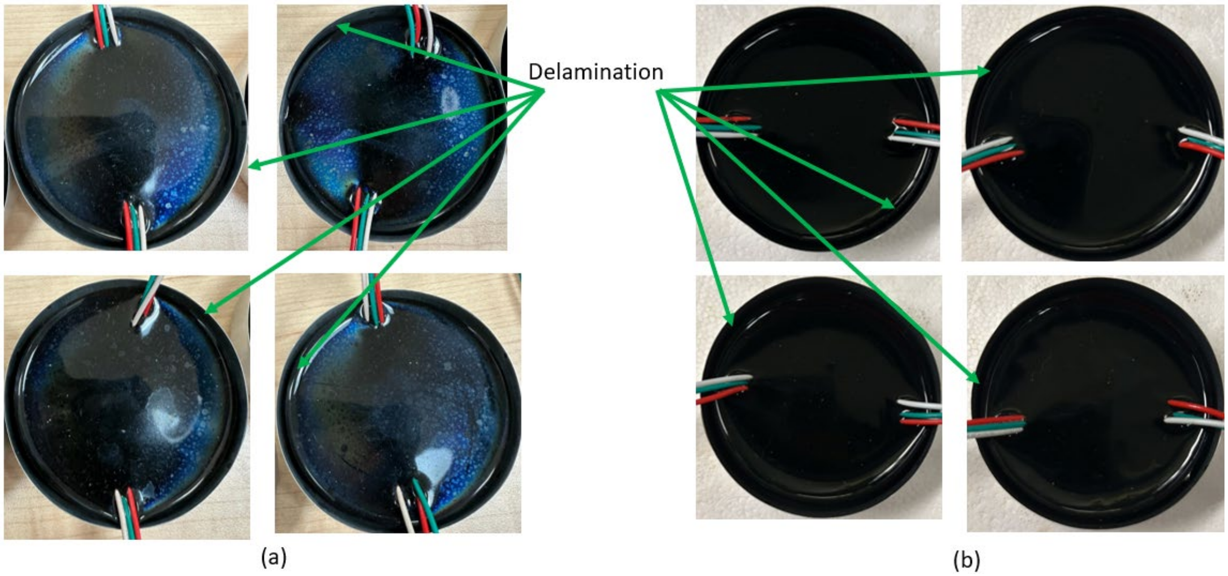

Figure 22: Delamination in Cx samples at (a) 85°C-85% RH and (b) 50°C-60% RH

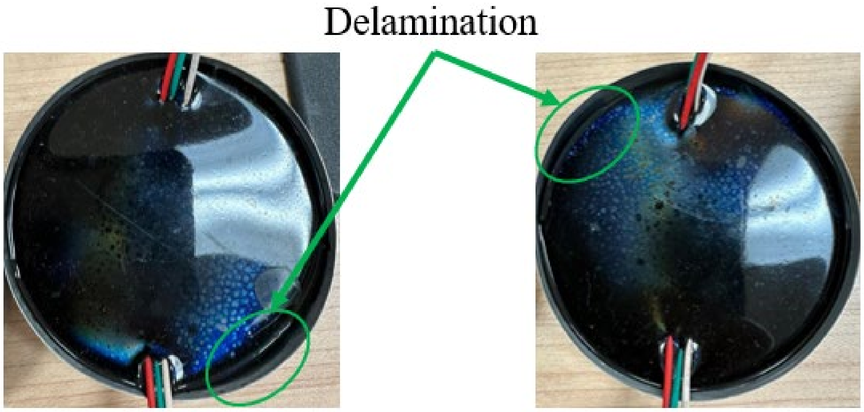

Cy 2

Cy 4

Figure 23: Delamination in Cy samples at 85°C-85% RH

4.2. Diffusion Modelling

Based on the experimental results, it is visually evident that the encapsulation materials and their composites follow the Fickian Diffusion Model. A one-dimensional Fick's law (1) for diffusion was used for curve fitting. Where C is the concentration of the diffusing substance, D is diffusivity, t is time, and x is the axis along the concentration gradient.

$$\frac{\partial C}{\partial t} = D\frac{\partial^2 C}{\partial t^2} \tag{1}$$

The boundary conditions for diffusion through a plane sheet were assumed, as stated in equation (2). Where C_0 is the initial concentration of moisture in the polymeric material, which is uniform across the material, C_1 is the constant concentration at the surface exposed to the moisture, L is the thickness of the plane sheet, and the moisture is impermeable at the bottom plane since it covered with aluminum sheet.

$$\begin{aligned} &C = C_0, \quad && t = 0, \quad && 0 < x < L \\ &C = C_1, \quad && t \leq 0, \quad && x = L \\ &\frac{\partial C}{\partial x} = 0, \quad && t \leq 0, \quad && x = 0 \end{aligned} \tag{2}$$

The combination of equation (1) and equation (2) gives out two analytical solutions for moisture concentration at a given time with equation (3) and equation (4). The first analytical solution (3) is useful for short periods, whereas the second corresponds to a longer time to reach equilibrium [25],[27].

$$\frac{C_t - C_0}{C_\infty - C_0} = \frac{M_t}{M_\infty} = 4\left(\frac{Dt}{L^2}\right)^{\frac{1}{2}}\left[\frac{1}{\pi^{\frac{1}{2}}} + 2\sum_{n=1}^{\infty}(-1)^n ierfc\frac{n}{2(Dt)^{\frac{1}{2}}}\right] \tag{3}$$

$$\frac{C_t - C_0}{C_\infty - C_0} = \frac{M_t}{M_\infty} = 1 - \sum_{n=1}^{\infty}\frac{8}{(2n+1)^2\pi^2} exp\left[\frac{-D((2n+1)^2\pi^2)t}{L^2}\right] \tag{4}$$

Where C_t is moisture concentration at time t, C_∞ is the equilibrium moisture concentration, M_t is moisture content at time t, and M_∞ is the equilibrium moisture content.

Equation (3) can be reduced to its first part, forming equation (5) to calculate a given material's diffusivity. Also, in isothermal conditions, equation (5) can be connected to the ratio of change in relative humidity at a time t and change in relative humidity to reach equilibrium—the combined equation in terms of moisture concentration, change in relative humidity, and moisture content.

$$\frac{C_t - C_0}{C_\infty - C_0} = \frac{\Delta RH_t}{\Delta RH_\infty} = \frac{M_t}{M_\infty} = 4\left(\frac{Dt}{\pi L^2}\right)^{\frac{1}{2}} \tag{5}$$

Based on the above equations, diffusion modeling was performed for curve fitting of the experimental data. The curve fitting was performed based on the diffusivity calculation, where the diffusivity was measured using relative humidity and moisture content change. The diffusivities were calculated based on equation (5) by using both moisture content and relative humidity, and the diffusivities of each of the samples have been recorded in Table 6. These diffusivities were then used in equation (4) to model the moisture ingression [32], [33].

	Test 1 (85°C-85% RH)		Test 2 (50°C-60% RH)	
Sample	Diffusivity with Moisture Content (m^2/s)	Diffusivity with RH (m^2/s)	Diffusivity with Moisture Content (m^2/s)	Diffusivity with RH (m^2/s)
Si 1	6.5511E-11	4.5393E-10	4.5027E-10	5.7265E-10
Si 2	6.3925E-11	4.2893E-10	2.7874E-10	5.0640E-10
Si 3	6.6984E-11	4.3014E-10	2.8315E-10	5.2662E-10
Si 4	7.2558E-11	4.8282E-10	2.8089E-10	5.6684E-10
Cx 1	5.4500E-11	1.2651E-10	2.8092E-11	2.1597E-10
Cx 2	4.6195E-11	1.0983E-10	3.1039E-11	1.6564E-10
Cx 3	4.2121E-11	1.5203E-10	2.5621E-11	2.0300E-10
Cx 4	5.1623E-11	1.3750E-10	3.2800E-11	1.6114E-10
Cy 1	4.2712E-11	4.3352E-11	2.2509E-11	1.5036E-10
Cy 2	4.5520E-11	4.1815E-11	2.3816E-11	1.1211E-10
Cy 3	2.8086E-11	5.8563E-11	2.4488E-11	1.1830E-10
Cy 4	4.3187E-11	4.7218E-11	2.3052E-11	1.0388E-10
Pu 1	1.3729E-11	3.2205E-11	1.5355E-11	5.5008E-11
Pu 2	1.0254E-11	3.9916E-11	1.6363E-11	5.7229E-11
Pu 3	1.0660E-11	4.4988E-11	1.6773E-11	3.6682E-11
Pu 4	1.7447E-11	3.4014E-11	1.7769E-11	4.4679E-11

Table 7: Calculated Diffusivities of samples in different methods

Figure 23 and Figure 24 display the results from applying diffusivities in equation (4). Compared with the diffusivities calculated from the relative humidity ratio, the diffusivities calculated by the moisture content are significantly lower as the mass loss was not accounted for. The trends in Figure 23 follow a similar path to the experimental results, whereas the trends in Figure 24 are scattered widely and take much more time to reach equilibrium.

As discussed in the previous chapter, due to mass loss in the polymers, the diffusivities calculated through moisture content have discrepancies in them. Further analysis of the mass loss through interdiffusion is required to determine the diffusivity accurately.

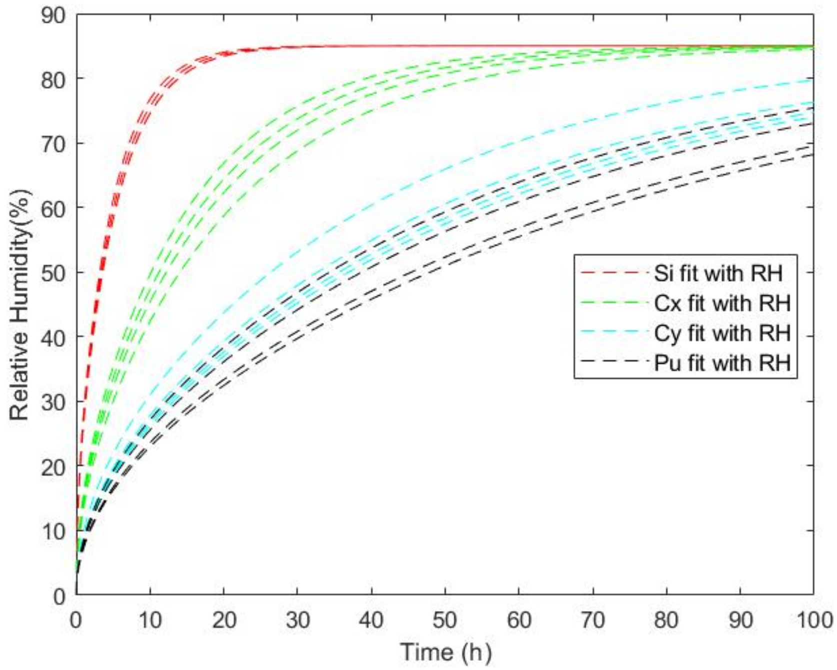

(a)

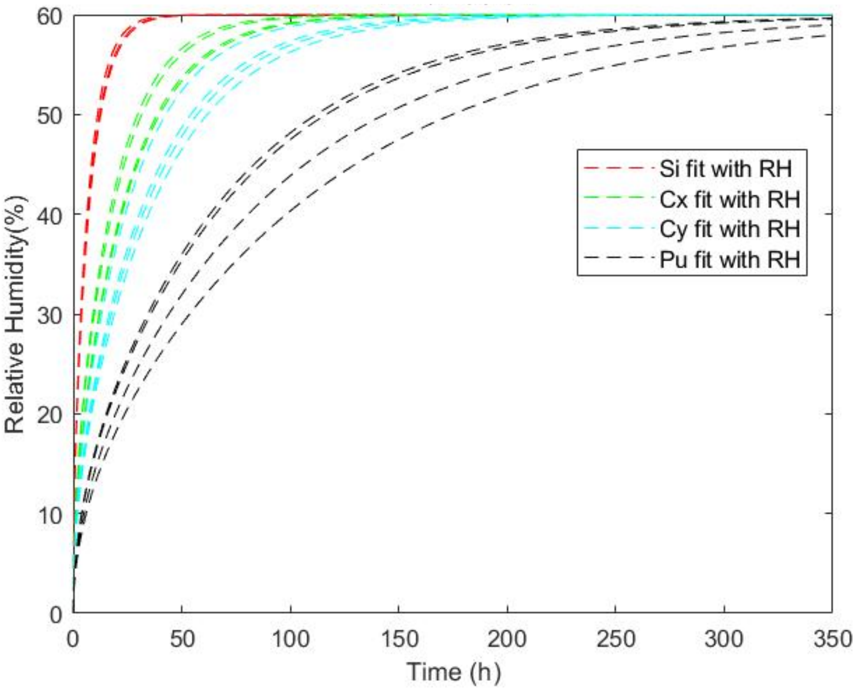

(b)

Figure 24: Curve Fitting using RH Diffusivity of the Samples at (a) 85°C-85% RH and (b) 50°C-60% RH

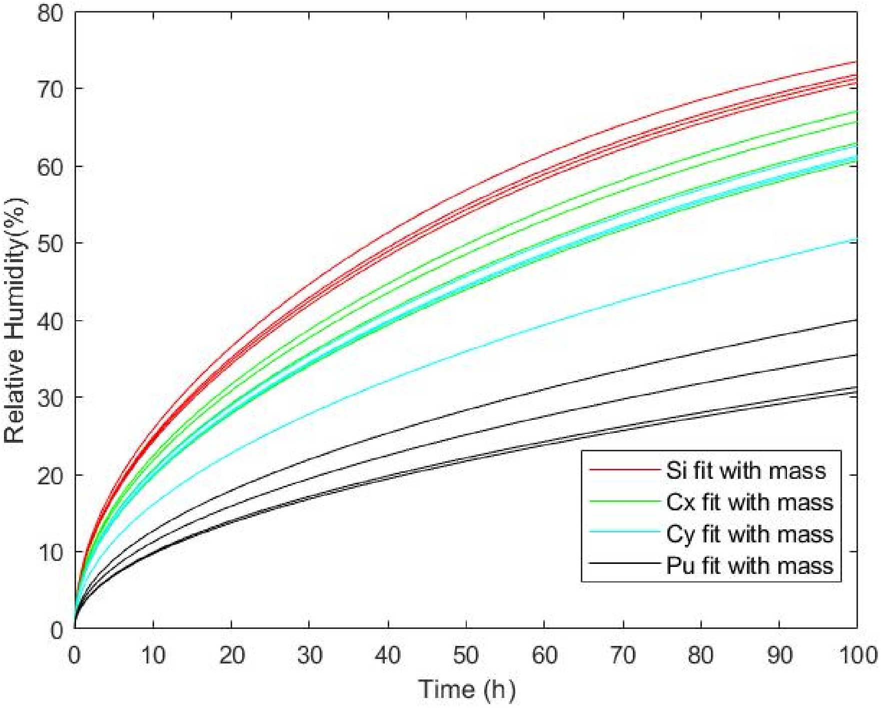

Relative Humidity(%)
Time (h)
0
10
20
30
40
50
60
70
80
90
100
Si fit with mass
Cx fit with mass
Cy fit with mass
Pu fit with mass

(a)

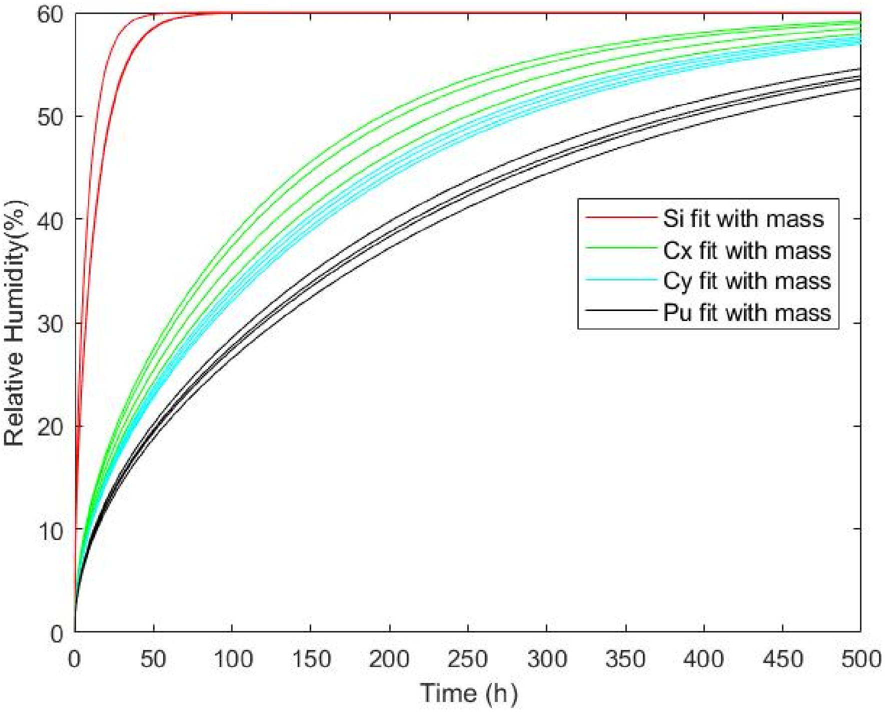

Relative Humidity(%)
Time (h)
0
50
100
150
200
250
300
350
400
450
500
10
20
30
40
60
Si fit with mass
Cx fit with mass
Cy fit with mass
Pu fit with mass

(b)

Figure 25: Curve Fitting using Moisture Content Diffusivity of the Samples at (a) 85°C-85% RH and (b) 50°C-60% RH

4.2.1. ANOVA Analysis of Diffusivity

The diffusivities for each of the samples were calculated with equation (5) based on relative humidity and moisture content, as shown in Table 6. The diffusivities calculated with the ratio of RH were found to be significantly lower than that of diffusivities with the moisture content ratio. This is due to the desorption of the water from the polymers when brought to room temperature, the delay in the mass measurements, and the mass loss in encapsulation materials. To further understand the diffusivities, ANOVA analysis was performed on each group set of the samples.

One-way ANOVA analysis was performed for each of the diffusivities sets, as mentioned in the table columns above, using the MATLAB function anova1. Further differentiation of every other group, post hoc ANOVA was performed using the Tukey-Kramer method.

Source	SS	df	MS	F	P value
Columns	6.10E-21	3	2.03E-21	68.3068	8.20E-08
Error	3.57E-22	12	2.98E-23		
Total	6.46E-21	15			

Table 8: ANOVA for Diffusivity with Moisture Content at 85-85 Test

Source	SS	df	MS	F	P value
Columns	4.47E-19	3	1.49E-19	566.8908	3.46E-13
Error	3.15E-21	12	2.63E-22		
Total	4.50E-19	15			

Table 9: ANOVA for Diffusivity with RH at 85-85 Test

Source	SS	df	MS	F	P value
Columns	2.71E-19	3	9.02E-20	50.211	4.58E-07
Error	2.16E-20	12	1.80E-21		
Total	2.92E-19	15			

Table 10: ANOVA for Diffusivity with Moisture content at 50-60 Test

Source	SS	df	MS	F	P value
Columns	5.79E-19	3	1.93E-19	340.9694	7.09E-12
Error	6.79E-21	12	5.66E-22		
Total	5.85E-19	15			

Table 11: ANOVA for Diffusivity with RH at 50-60 Test

Based on ANOVA analysis of each group set, the large value of F-statistic and low P-value suggests that all the data sets in a group set are significantly different from each other. Further investigation with post hoc analysis was performed for a pair-wise comparison of every sample set. The “Multcompare” function in MATLAB with the “Tukey-Kramer” method was used to determine the statistically significant mean difference between the pairs of data sets, as shown in Figure 25 and Figure 26. In Figure 25 (a), it was found that the diffusivities of Cx and Cy are not statistically different, but contrastingly, in Figure 25 (b), by using the RH model, the diffusivities of Cy and Pu are not statistically different. It was observed that, except for the abovementioned pairs, every other data set pair was statistically different from each other in the first test. Figure 26 (a) shows that the diffusivities of Cx, Cy, and Pu are statistically similar, but in Figure 26 (b), all the sample sets of diffusivities are statistically different.

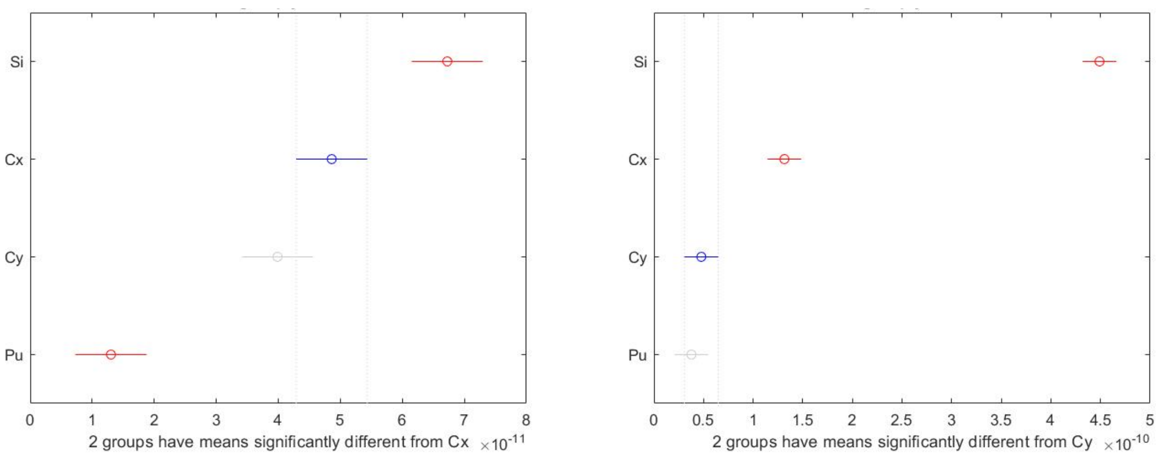

(a) (b)

Figure 26: Post hoc analysis using the Tukey-Kramer method for Diffusivity at 85-85 Test with (a) Moisture Content and (b) RH

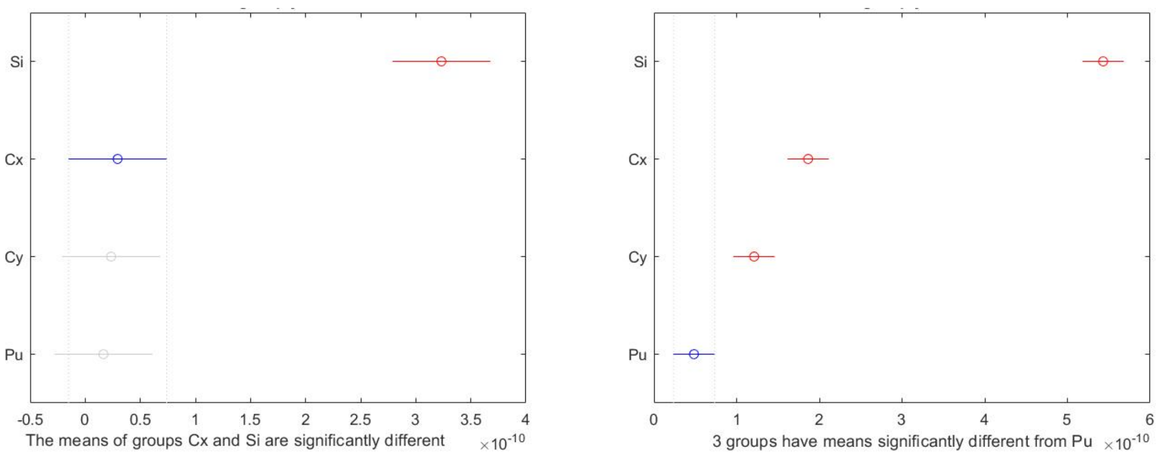

(a) (b)

Figure 27: Post hoc analysis using the Tukey-Kramer method for Diffusivity at 50-60 Test with (a) Moisture Content and (b) RH

4.3. Failure Analysis and Thermomechanical Analysis of GaN Devices

4.3.1. Failure Analysis of GaN MOSFETs

EPC2001C MOSFETs were the primary devices in a dual-active-bridge (DAB) based DC-AC microinverter for residential PV systems. To assess the reliability of the microinverter, it was subjected to an unpowered thermal cycling test. The maximum and minimum temperatures for cycling were taken as 105°C and -40°C with a dwell time of 11 hours each. Failure in the primary devices was observed between 800-1000 hours of testing. The failures were confirmed by electrical testing.

The failure analysis of these GaN switches was performed by a confocal scanning acoustic microscope (C-SAM) using OKOS NDT CF-300 Acoustic Microscope. The scans revealed that the solder bumps had delaminated from the board, causing an open circuit at the gate, source, and drain pads, as shown in Figure 27. A thermomechanical simulation was performed on these chips to investigate the root cause of the failure. Given that delamination had occurred in the solder bumps of flip-chip packages, the analysis primarily focused on comprehending the behavior of these solder bumps under thermal loading.

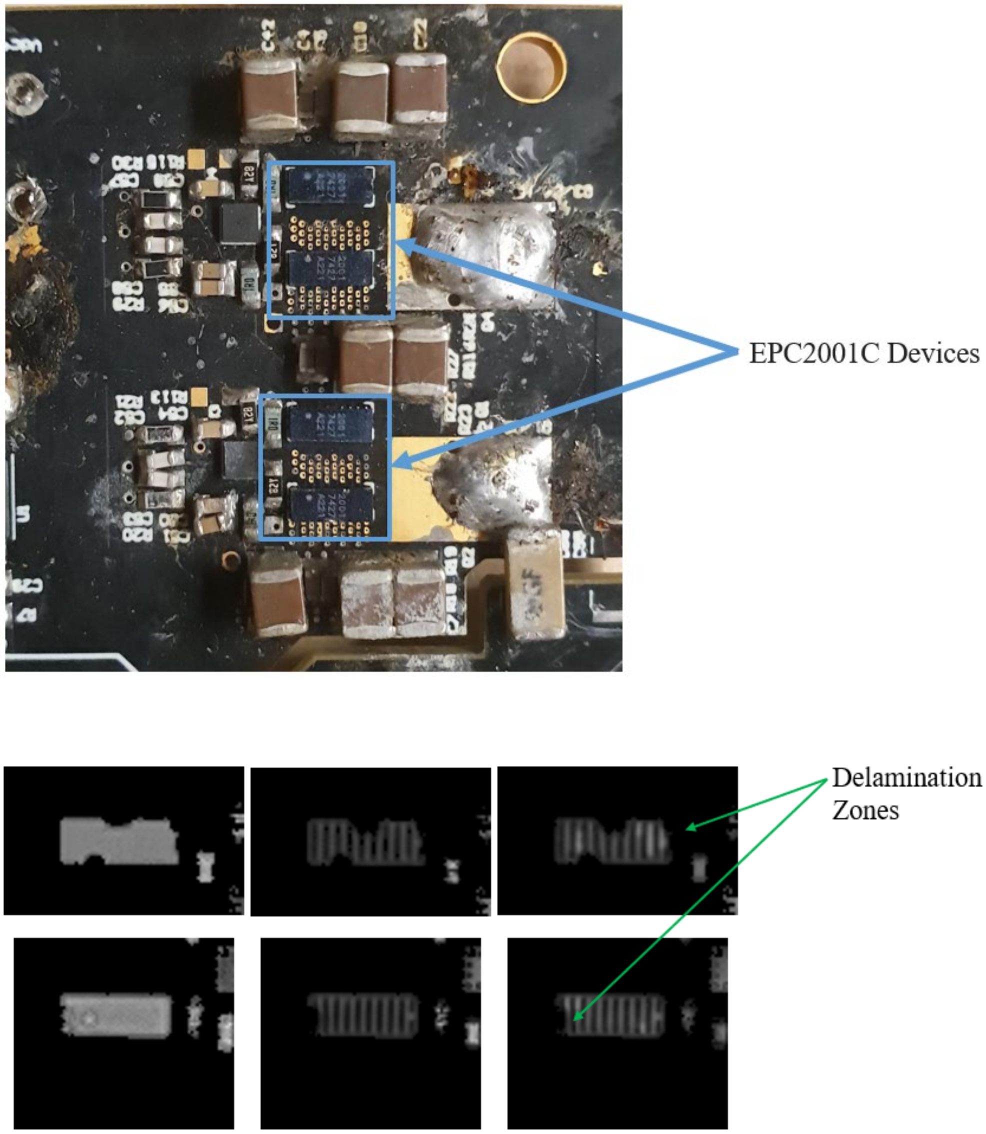

Figure 28: Failure Analysis of GaN MOSFETs to locate the delaminated solder bumps

4.3.2. Thermo-mechanical Parametric Investigation of Potting Materials

Thermo-mechanical analysis was performed on different GaN power MOSFETs EPC2201C and EPC2204. Due to a shortage in the supply, EPC2001C switches were replaced by EPC2204 switches, and thermomechanical analysis was performed on both devices. These MOSFETs were subjected to a temperature load of 105°C to determine the effects on stresses and strains experienced by the solder bumps in these packages. These packages are asymmetric land grid array (LGA) flip-chip devices. This flip-chip technology is similar to a ball grid array (BGA). Visually, these solder balls are extended to form solder hemi cylinders.

These devices were simulated at high-temperature loading and were tested to determine the best potting and underfill encapsulation for maximum reduction of the stresses and strains. The simulation was performed in two stages. In the preliminary stage, combinations of silicone and epoxy encapsulations were iteratively swapped for potting and underfill encapsulations, along with simulation without any potting material or underfill. In later stages, the properties of epoxy were kept constant for underfill, and different polymeric potting encapsulation materials were simulated, which will be discussed in detail in the latter part of this chapter.

The GaN MOSFETs were modeled using SolidWorks, and the design was imported into the ANSYS workbench, as shown in Figure 28. The components were subjected to the thermal load in a static structural analysis system. The mesh was created using multizone mesh at the solders, and a thermal load of 105°C was given to the assembly, which was ramped up in 1 hour. Since the package was asymmetric, the neutral planes were assumed at the two-side surfaces of the packages, and the fixed support was given to the bottom corner point of the FR-4 laminate [34]. A forced conversion model was used for the solutions.

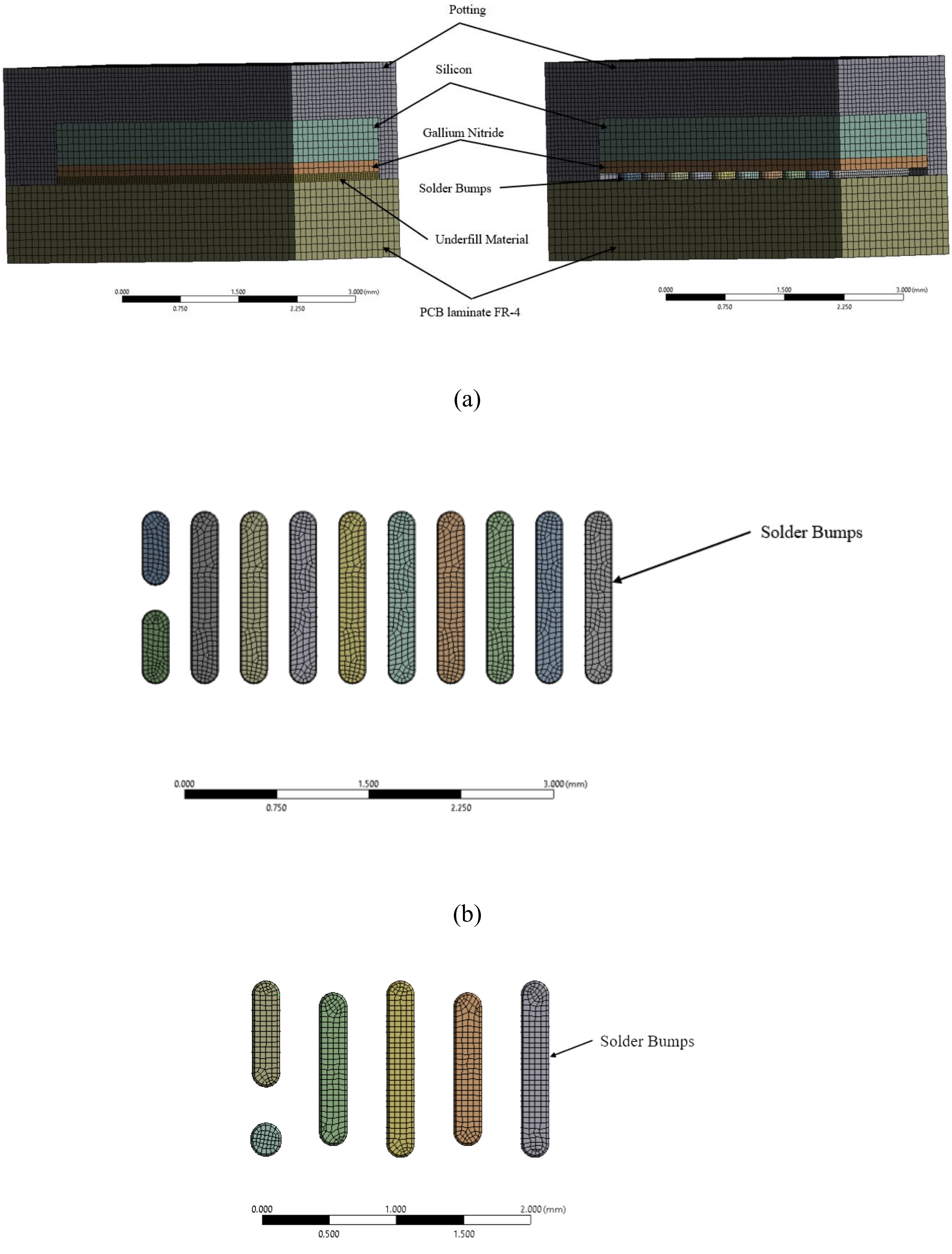
Potting
Silicon
Gallium Nitride
Solder Bumps
Underfill Material
PCB laminate FR-4
0.000
1.500
3.000 (mm)
0.750
2.250
Solder Bumps
0.000
1.500
3.000 (mm)
0.750
2.250
Solder Bumps
0.000
1.000
2.000 (mm)
0.500
1.500

(a)

(b)

(c)

Figure 29: Modelling and meshing of GaN Devices (a) Assembly, (b) EPC2001C solder bumps, and (c) EPC2204 solder bumps

The simulation results include deformation, normal, and shear stresses concentrated on the solder bumps. The analysis was performed using Butyl Rubber, Thermoplastic Olefin (TPO), Styrene Butadiene (SBR) and Ethylene-vinyl acetate (EVA) along with Polyurethane, epoxy resin and silicone. The material properties were taken from the ANSYS engineering data. A comparison between the change from EPC2001C to EPC2204 for the primary switches is demonstrated in Figure 29. Based on the results, the overall deformation and shear stress were observed to be lower in EPC2204 in comparison with EPC2001C. However, the normal stresses were observed to be higher in EPC2204. Due to the difference in the dimensions of the switches, i.e., EPC2204 is smaller when compared to EPC2001C, and also, the asymmetry of the solder bumps in EPC2204 raises out-of-plane stresses, causing normal stress to increase.

In the case of EPC2001C, the application of the potting and underfill material significantly reduced the stresses on the solder bumps. The application of the underfill material significantly reduced both normal and shear stresses in comparison with the naked chips. In the case of potting material alone, the normal stress tends to increase due to insufficient support around the solder bumps. Overall, the application of potting and underfill reduces the normal stresses in a similar trend. However, the shear stresses observed by the application of silicone and EVA potting reduce an extra 5 MPa when compared with other encapsulation materials.

When compared to different materials, the application of silicones as potting encapsulation significantly reduces the stresses experienced by the solder bumps. Also, as the thermal properties and ease in the application of the silicone outstands the other materials.

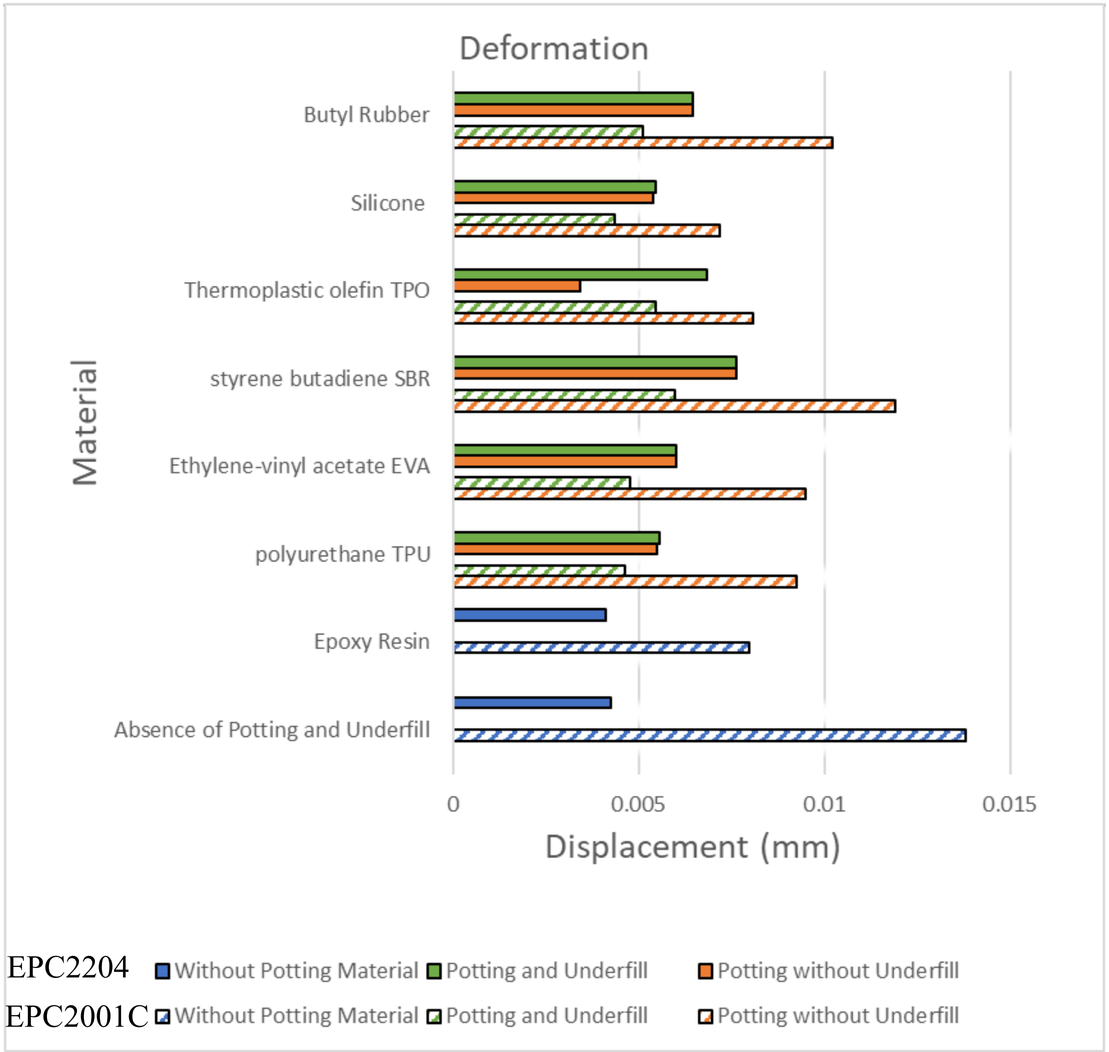

(a)

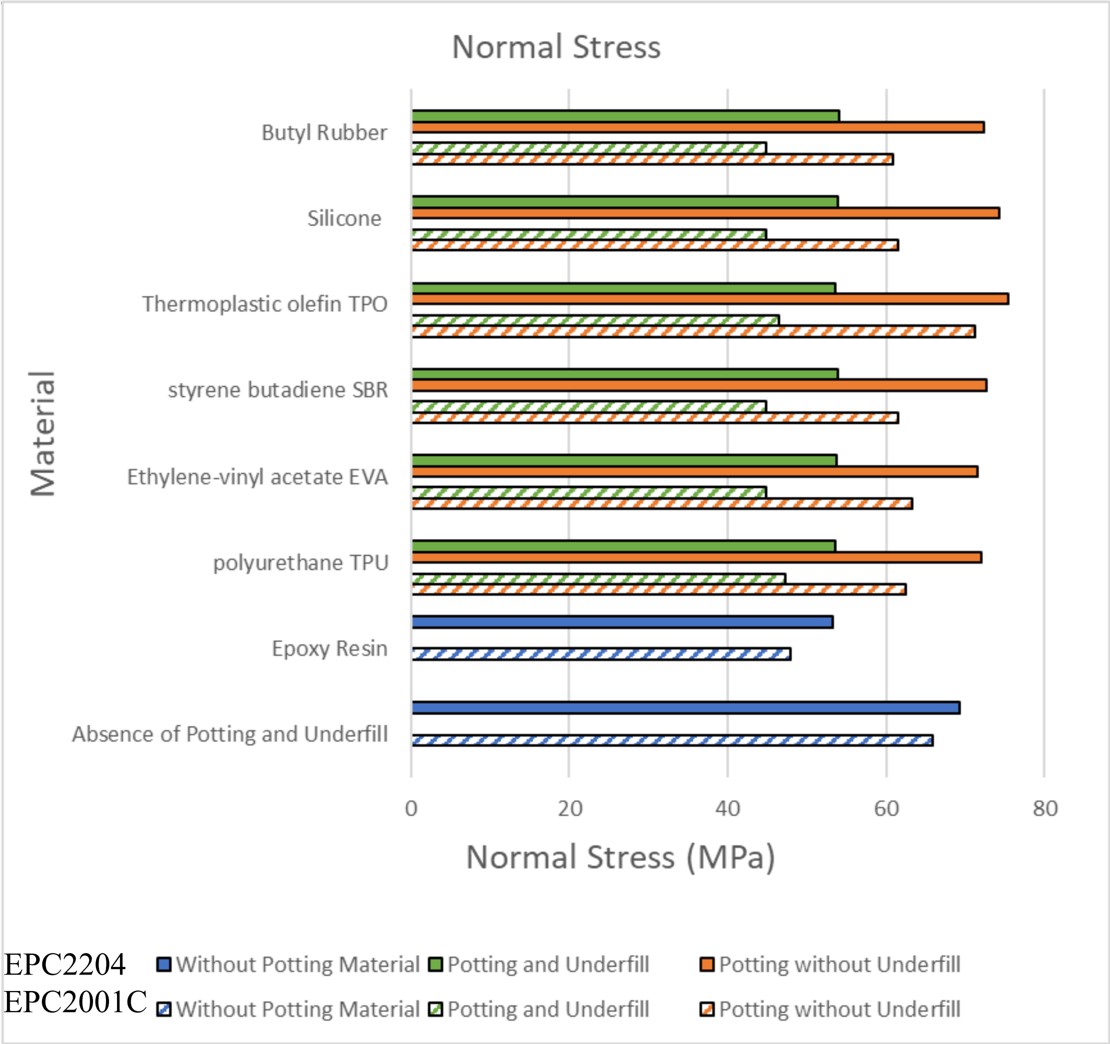
Normal Stress
Material
Butyl Rubber
Silicone
Thermoplastic olefin TPO
styrene butadiene SBR
Ethylene-vinyl acetate EVA
polyurethane TPU
Epoxy Resin
Absence of Potting and Underfill
0
20
40
60
80
Normal Stress (MPa)
EPC2204
Without Potting Material
Potting and Underfill
Potting without Underfill
EPC2001C
Without Potting Material
Potting and Underfill
Potting without Underfill

(b)

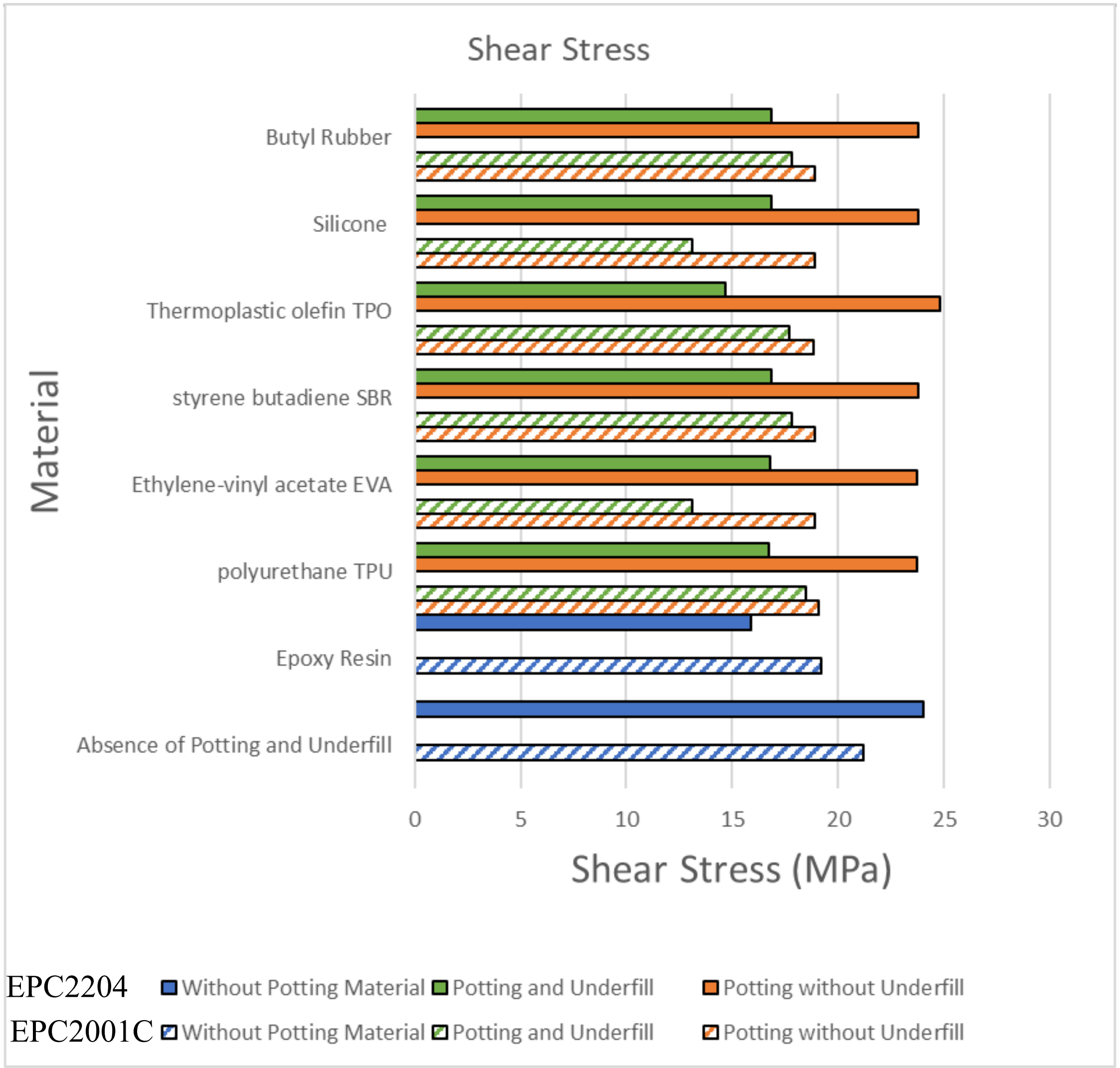

(c)

Figure 30: Simulation results of GaN switches (a) Deformation, (b) Normal stress, and (c) Shear stress

5. Contributions and Future Work

5.1. Contributions

The thesis aimed to develop an economical and simple method for establishing a moisture barrier on silicone encapsulation. The thesis demonstrates that the goal was successfully achieved by encapsulating a laminated moisture barrier of polyurethane on silicone. The outcome of this encapsulation process effectively enhanced the moisture impermeability of the silicone material.

A literature review was performed on moisture-induced failures in silicone-encapsulated power electronic modules and testing procedures. Two of the testing procedures were conducted and compared, and the procedure with embedded sensors was found to be more accurate as it accounts for moisture permeability and mass loss.

Failure analysis of GaN MOSFETs was performed, and thermo-mechanical simulations were performed to determine stresses and strains on solder bumps. Additionally, a study of thermomechanical analysis was conducted to minimize stresses and strains on the solder bumps by applying potting and underfill materials.

5.2. Future Work

Expanding on existing research, this chapter delves deeper into future work, adding more insights to our understanding. Firstly, the tests performed in this study account only for the encapsulation materials. Testing can be performed on actual electronic modules by applying composite encapsulation materials. This investigation comprehends the effectiveness of the new composite for protecting electronic modules from moisture while identifying the failure mechanisms that may arise with the new composites.

This thesis accounts for two environmental conditions for the comparison of diffusivities. More tests can be performed to determine a spectrum of diffusivities with changes in environmental temperature and relative humidity. This gives a broader understanding of the environmental effects on the diffusivity of the encapsulation materials. Along with the environmental effects, a study on the thickness of the polyurethane protective layer can be performed, and the optimum thickness can be achieved for a given environmental condition.

Testing can be performed by cycling the moisture ingression until sample saturation to understand further degradation effects on the diffusivities of these materials. After complete exposure to moisture, until the materials reach complete saturation, the samples can be dehydrated and exposed to moisture again to observe the diffusivity change.

A detailed simulation can be performed to understand the environmental effects on the performance of the moisture barrier. The new simulation can include hygroscopic swelling of the materials. The mismatch due to hygroscopic swelling along with CTE mismatches can cause delamination of the moisture barrier.

Appendix

Arduino script for Multiplexer

```
#include <Wire.h>

int i;

float myTime;

float t=millis();

void setup() {

  for(i=2; i<=13;i++){

  pinMode(i, OUTPUT);

  }

  for(i=22; i<=27;i++){

  pinMode(i, OUTPUT);

  digitalWrite(i, LOW);

  }

  Wire.begin();        // join i2c bus (address optional for master)

  Serial.begin(9600);  // start serial for output

}



void loop() {
```

```
for(i=2; i<=13;i++){
digitalWrite(i, HIGH); // Turn the CE on
delay(30);
uint8_t Byte[0];
uint16_t temp;
uint16_t humid;
double humidity_1;
double temprature_1;
double humidity_2;
double temprature_2;
Wire.beginTransmission(byte(0x7F)); // transmit to device #127 (0x7F)
Wire.write(byte(0x01));      // sets register pointer to the command register (0x00)
Wire.write((00000001));
Wire.endTransmission();
delay(50);
Wire.beginTransmission(byte(0x7F));
Wire.write(byte(0x04));
Wire.endTransmission();
```

```
delay(50);

Wire.requestFrom(0x7F,4);

bool flag = true;

while(flag)

{

  if (4 <= Wire.available())

  {

    Byte[0] = Wire.read();

    Byte[1] = Wire.read();

    Byte[3] = Wire.read();

    Byte[4] = Wire.read();

    humid = ((unsigned int ) Byte[1] << 8 | Byte[0]);

    temp = ((unsigned int ) Byte[4] << 8 | Byte[3]);

    temprature_1=((double)(temp-774)*(0.1));

    humidity_1=((double)(humid)*(100)/1024);

    flag = false;

}

  else{
```

```
     goto prop1;
   }
 }

 Serial.print("Sensor ");
 Serial.print(i);
 Serial.print(":");
 Serial.print(",");
 delay(5);
 t=millis()/1000;
 Serial.print(t);
 Serial.print(",");
 delay(5);
 Serial.print(humidity_1);
 Serial.print(",");
 delay(5);
 Serial.print(temprature_1);
 Serial.print("\n");
```

```
delay(5);

prop1:

digitalWrite(i, LOW);

delay(1000);

}

for(i=22; i<=26;i++){

digitalWrite(i, HIGH); // Turn the CE on

delay(30);

uint8_t Byte[0];

uint16_t temp;

uint16_t humid;

double humidity_1;

double temprature_1;

double humidity_2;

double temprature_2;

Wire.beginTransmission(byte(0x7F)); // transmit to device #127 (0x7F)

Wire.write(byte(0x01));      // sets register pointer to the command register (0x00)

Wire.write((00000001));
```

```
Wire.endTransmission();

delay(50);

Wire.beginTransmission(byte(0x7F));

Wire.write(byte(0x04));

Wire.endTransmission();

delay(50);

Wire.requestFrom(0x7F,4);

bool flag = true;

while(flag)

{

  if (4 <= Wire.available())

  {

    Byte[0] = Wire.read();

    Byte[1] = Wire.read();

    Byte[3] = Wire.read();

    Byte[4] = Wire.read();

    humid = ((unsigned int ) Byte[1] << 8 | Byte[0]);

    temp = ((unsigned int ) Byte[4] << 8 | Byte[3]);
```

```
    temprature_1=((double)(temp-774)*(0.1));

    humidity_1=((double)(humid)*(100)/1024);

    flag = false;

  }

  else{

    goto prop2;

  }

}

Serial.print("Sensor ");

Serial.print(i);

Serial.print(":");

Serial.print(",");

delay(5);

t=millis()/1000;

Serial.print(t);

Serial.print(",");

delay(5);

Serial.print(humidity_1);
```

```
  Serial.print(",");

  delay(5);

  Serial.print(temprature_1);

  Serial.print("\n");

  delay(5);

  prop2:

  digitalWrite(i, LOW);

  delay(1000);

  }

  delay(10000);

 }
```

References

[1] Copernicus Climate Change Service, “ERA5: Fifth Generation of ECMWF Atmospheric Reanalyses of the Global Climate.”

[2] Y. H. Lee, I. Chin, and W. K. Loh, “Electronic Packaging Moisture Interaction Study,” in *2018 IEEE 38th International Electronics Manufacturing Technology Conference (IEMT)*, IEEE, Sep. 2018, pp. 1–8. doi: 10.1109/IEMT.2018.8511674.

[3] İ. Baylakoğlu *et al.*, “The detrimental effects of water on electronic devices,” *e-Prime - Advances in Electrical Engineering, Electronics and Energy*, vol. 1, p. 100016, 2021, doi: 10.1016/j.prime.2021.100016.

[4] A. Shrivastava, M. H. Azarian, and M. Pecht, “Failure of Polymer Aluminum Electrolytic Capacitors Under Elevated Temperature Humidity Environments,” *IEEE Trans Compon Packaging Manuf Technol*, vol. 7, no. 5, pp. 745–750, May 2017, doi: 10.1109/TCPMT.2017.2658446.

[5] W. W. Sheng and R. P. Colino, “Power Electronic Modules: Design and Manufacture,” 2004. [Online]. Available: https://api.semanticscholar.org/CorpusID:107517137

[6] S. A. Meguid, C. Zhuo, and F. Yang, “Effective Mitigation of Shock Loads in Embedded Electronic Packaging Using Bilayered Potting Materials,” *J Electron Packag*, vol. 136, no. 4, Dec. 2014, doi: 10.1115/1.4026542.

[7] H. Ardebili and M. Pecht, *Encapsulation Technologies for Electronic Applications*. 2018.

[8] K. Otsuka, Y. Takeo, T. Yamada, S. Kuroda, and H. Tachi, “The Mechanisms that Provide Corrosion Protection for Silicone Gel Encapsulated Chips,” *IEEE Transactions on*

Components, Hybrids, and Manufacturing Technology, vol. 10, no. 4, pp. 666–671, Dec. 1987, doi: 10.1109/TCHMT.1987.1134772.

[9] J. J. Shea, "Electronic Packaging Materials and their Properties," *Electrical Insulation Magazine, IEEE*, vol. 17, pp. 60–60, Sep. 2001, doi: 10.1109/MEI.2001.954592.

[10] Yoshimichi Takei *et al.*, "Unique high reliability urethane resin for car electronic module packaging," in *2008 IEEE 9th VLSI Packaging Workshop of Japan*, IEEE, Dec. 2008, pp. 109–112. doi: 10.1109/VPWJ.2008.4762224.

[11] C. Zorn and N. Kaminski, "Temperature Humidity Bias (THB) Testing on IGBT Modules at High Bias Levels," in *CIPS 2014; 8th International Conference on Integrated Power Electronics Systems*, 2014, pp. 1–7.

[12] C. Zorn and N. Kaminski, "Acceleration of temperature humidity bias (THB) testing on IGBT modules by high bias levels," in *2015 IEEE 27th International Symposium on Power Semiconductor Devices & IC's (ISPSD)*, IEEE, May 2015, pp. 385–388. doi: 10.1109/ISPSD.2015.7123470.

[13] C. Papadopoulos, C. Corvasce, A. Kopta, D. Schneider, G. Pâques, and M. Rahimo, "The influence of humidity on the high voltage blocking reliability of power IGBT modules and means of protection," *Microelectronics Reliability*, vol. 88–90, pp. 470–475, 2018, doi: https://doi.org/10.1016/j.microrel.2018.07.130.

[14] B. T. DeBoi, B. W. Nelson, P. Kanatzar, F. Fraas, A. Curbow, and T. McNutt, "Analysis of Moisture-Induced Void Formations within Silicon Carbide Power Modules," in *PCIM Europe 2023; International Exhibition and Conference for Power Electronics, Intelligent*

Motion, Renewable Energy and Energy Management, 2023, pp. 1–8. doi: 10.30420/566091121.

[15] P. U. 2013 ASTM International: West Conshohocken, "ASTM F1249-20; Standard Test Method for Water Vapor Transmission Rate Through Plastic Film and Sheeting Using a Modulated Infrared Sensor." 2013.

[16] G. Jorgensen, K. Terwilliger, S. Glick, J. Pern, and T. McMahon, "Materials Testing for PV Module Encapsulation," Sep. 2003.

[17] S. J. Sung, J. Park, Y. S. Cho, S. H. Gihm, S. J. Yang, and C. R. Park, "Enhanced gas barrier property of stacking-controlled reduced graphene oxide films for encapsulation of polymer solar cells," *Carbon N Y*, vol. 150, pp. 275–283, 2019, doi: https://doi.org/10.1016/j.carbon.2019.04.120.

[18] C. Il Jo, J. Ko, Z. Yin, Y.-J. Kim, and Y. S. Kim, "Solvent-Free and Highly Transparent SiO2 Nanoparticle–Polymer Composite with an Enhanced Moisture Barrier Property," *Ind Eng Chem Res*, vol. 55, no. 35, pp. 9433–9439, 2016, doi: 10.1021/acs.iecr.6b01470.

[19] H. Ardebili, C. Hillman, M. A. E. Natishan, P. McCluskey, M. G. Pecht, and D. Peterson, "A comparison of the theory of moisture diffusion in plastic encapsulated microelectronics with moisture sensor chip and weight-gain measurements," *IEEE Transactions on Components and Packaging Technologies*, vol. 25, no. 1, pp. 132–139, Mar. 2002, doi: 10.1109/6144.991185.

[20] M. G. Pecht, H. Ardebili, A. A. Shukla, J. K. Hagge, and D. Jennings, "Moisture ingress into organic laminates," *IEEE Transactions on Components and Packaging Technologies*, vol. 22, no. 1, pp. 104–110, Mar. 1999, doi: 10.1109/6144.759359.

[21] K. Li, B. Zhang, Z. Yang, X. Jiang, and X. Li, “Degradation behaviors of silicone gel encapsulation material with moisture intrusion,” *Polym Degrad Stab*, vol. 206, p. 110197, 2022, doi: https://doi.org/10.1016/j.polymdegradstab.2022.110197.

[22] N. Kyranaki, M. Jankovec, M. Topic, R. Gottschalg, and T. Betts, “Investigation of Moisture Ingress and Egress in Polymer -Glass Laminates for PV Encapsulation,” Sep. 2019.

[23] K. Zhang, G. Schlottig, E. Mengotti, O. Quittard, and F. Iannuzzo, “Study of moisture transport in silicone gel for IGBT modules,” *Microelectronics Reliability*, vol. 114, p. 113773, 2020, doi: https://doi.org/10.1016/j.microrel.2020.113773.

[24] M. Jankovec *et al.*, “In-Situ Monitoring of Moisture Ingress in PV Modules Using Digital Humidity Sensors,” *IEEE J Photovolt*, vol. 6, no. 5, pp. 1152–1159, Sep. 2016, doi: 10.1109/JPHOTOV.2016.2583779.

[25] Z. An, K. Chen, W. Huang, X. Wang, F. Zheng, and Y. Zhang, “Moisture Barrier Properties of Silicone Rubber Surface Layers Fluorinated at Different Temperatures,” *IEEE Transactions on Dielectrics and Electrical Insulation*, vol. 28, no. 1, pp. 82–89, Feb. 2021, doi: 10.1109/TDEI.2020.009023.

[26] W.-H. Liao *et al.*, “Effect of silane-functionalized TiO2 on the optical properties and moisture barrier of silicone resin nanocomposites,” *RSC Adv.*, vol. 4, no. 73, pp. 38614–38622, 2014, doi: 10.1039/C4RA04477K.

[27] S. Lee, J.-Y. Hong, and J. Jang, “Multifunctional Graphene Sheets Embedded in Silicone Encapsulant for Superior Performance of Light-Emitting Diodes,” *ACS Nano*, vol. 7, no. 7, pp. 5784–5790, 2013, doi: 10.1021/nn4024587.

[28] C. Shea, B. Moloznik, and D. Hemmelgarn, “Printing and Profiling Fine Feature Devices,” 2003. [Online]. Available: https://api.semanticscholar.org/CorpusID:110834495

[29] J. O’brien, “Factors Affecting the Mechanical Strength of Reflowed Solder Joints for Surface Mount Technology (SMT) Products,” *Accessed: Aug. 06, 2023. [Online]. Available:https://www.pemnet.com/eu/wpcontent/uploads/sites/10/2022/06/Factors_Affecting_Mechanical_Strength_WhitePaper.pdf.*

[30] K. Dusek, M. Novak, and A. Rudajevova, “Study of the components self-alignment in surface mount technology,” in *2012 35th International Spring Seminar on Electronics Technology*, IEEE, May 2012, pp. 197–200. doi: 10.1109/ISSE.2012.6273138.

[31] R. S. S. Kumari and C. Gayathri, “Interfacing of MEMS motion sensor with FPGA using I2C protocol,” in *2017 International Conference on Innovations in Information, Embedded and Communication Systems (ICIIECS)*, IEEE, Mar. 2017, pp. 1–5. doi: 10.1109/ICIIECS.2017.8275932.

[32] John Crank, *The mathematics of diffusion*. 2001.

[33] T.-W. Chang, C. H. Wang, and C.-L. Tsai, “Advancing Boundary Model for Moisture Diffusion in A Composite Laminate,” *J Compos Mater*, vol. 42, no. 10, pp. 957–973, 2008, doi: 10.1177/0021998308088612.

[34] M. Serebreni, P. McCluskey, D. Hillman, N. Blattau, and C. Hillman, “Experimental and Numerical Investigation of Underfill Materials on Thermal Cycle Fatigue of Second Level Solder Interconnects Under Mean Temperature Conditions,” in *ASME 2018 International Technical Conference and Exhibition on Packaging and Integration of Electronic and*

Photonic Microsystems, American Society of Mechanical Engineers, Aug. 2018. doi: 10.1115/IPACK2018-8338.